ENERGY DEPOSITION AND NANODOSIMETRY OF IODINE-125 AND TIN-117M LABELED GOLD NANOPARTICLES: A COMPUTATIONAL MODEL USING GEANT4-DNA

A Thesis

by

MARINA LEE PULLEY

Submitted to the Office of Graduate and Professional Studies of
Texas A&M University
in partial fulfillment of the requirements for the degree of

MASTER OF SCIENCE

Chair of Committee,	Gamal Akabani
Committee Members,	John Ford
	Charles M. Folden III
Head of Department,	Yassin Hassan

August 2015

Major Subject: Health Physics

ABSTRACT

Micro-metastases are a significant problem in cancer therapy. These are cell clusters that can be found throughout the body, often arising from the primary tumor. They can go on to form radiologically discernable metastases. Our understanding of metastatic cancer is evolving, and therapeutic strategies need to evolve with it.

Gold nanoparticles have been extensively used in the medical field. In this study, gold nanoparticles containing Auger emitting radionuclides of ^{125}I or ^{117m}Sn were modeled for the treatment of micro-metastatic cancer. The Monte Carlo transport code Geant4-DNA was used to model the decay of these radioactive atoms, following each of the emissions along its particle track down to thermal energies. This open source "track structure" code was able to keep a detailed spatiotemporal report of energy depositions and secondary particle formation. The energy deposition data generated was visualized using the software VisIt.

It was found that both radionuclides contained adequate energy for the treatment of circulating tumor cells and micro-metastases. However, depending upon micro-metastatic tumor volume, they have different benefits. The energy deposition from ^{125}I is much denser overall when there are a large number of decays. Compared to that, ^{117m}Sn has a less dense energy deposition for a large number of decays, but individual decays were generally a higher energy.

The present analysis showed that very low energy electrons will not escape from the gold nanoparticle itself; they would excite tertiary particles and create thermal energy themselves, on the order of a few eV. The cascade of electrons generates what is

commonly referred to as a Coulomb explosion, inducing significant direct damage to molecules adjacent to the gold nanoparticle. The electrons that escape the gold nanoparticle would go on to also induce direct damage to the DNA if the particle is within several angstroms, or create free radicals if it is not. Based on the number of free radicals generated, indirect damage to the DNA of the cancerous lesion would also be quite substantial. The resulting dose enhancement indicates that use of radioactive gold nanoparticles for the therapeutic treatment of micro-metastatic cancer can be an excellent treatment strategy.

ACKNOWLEDGEMENTS

I would like to thank my advisor, Dr. Akabani, for always helping and encouraging me to do the best work I'm capable of. I would also like to thank the rest of my committee who took their time to support me. Last, but certainly not least, I would like to thank my family and friends who have supported me through this crazy, wonderful chapter of life.

NOMENCLATURE

atm	Standard Atmosphere
CPP	Cell Penetrating Peptides
CTC	Circulating Tumor Cells
CSDA	Continuous Slowing Down Approximation
EC	Electron Capture
eV	Electron Volt
FDA	Food and Drug Administration
d	Day
h	Hour
keV	Kiloelectron Volt
LET	Linear Energy Transfer
MeV	Megaelectron Volt
μA	Micro Amperes
MM	Micro-metastases
nm	Nanometer
NNDC	National Nuclear Data Center
PET	Positron Emission Tomography
RBE	Relative Biological Effectiveness
s	Second
SPECT	Single-Photon Emission Computed Tomography

TABLE OF CONTENTS

LIST OF FIGURES

LIST OF TABLES

1. INTRODUCTION

1.1 Cancer Metastases

The Center for Disease Control reported that 117 million Americans were living with at least one chronic disease in 2012 (*1*). The two most common chronic diseases, heart disease and cancer, make up 48% of fatalities across the nation (*2*). The medical expenses associated with these diseases makes up about 75% of the total medical charges in the country (*3*). In 2010, the cost of cancer was more than $120 billion, according to the National Cancer Institute (*4*).

There have been significant advances in understanding the etiology and treatment of cancer, however the incidence and prevalence of cancer have not changed considerably in the last decade. There are 14.5 million Americans living with cancer, and 1.6 million new cancer cases will be diagnosed this year (*5*). It is expected that approximately 0.6 million people will die of cancer in 2015, or about 1600 people per day (*6*).

Cancer treatment is a complex process that requires a clear understanding of organs, tissues and tumor anatomy, physiology and immunology. The primary form of treatment is surgery (surgical resection) followed by chemotherapy and external beam radiotherapy or chemo-radiotherapy. However, approximately 70% of all patients with cancer will develop metastases (*7*). Cancer deaths tend to occur as a secondary symptom of cancer metastases.

The treatment of metastatic cancer is a significant economical burden, as the disease becomes unmanageable and terminal in most patients. Therefore, metastases are the final frontier in cancer progression.

Breast cancer is the most prevalent form of cancer in women, affecting about 12.5% of the population (*8*). This cancer, specifically, is a burden on the US healthcare system resources. The National Cancer Institute projects that 17% of the more than 200,000 women will die of breast cancer this year alone (*5*). Breast cancer will metastasize in about 30% of the patients, and the survival time is only a maximum of three years after that (*9*). Therapeutic strategies for this cancer are expensive, intensive and complex. The Food and Drug Administration (FDA) has approved more than a half a dozen drugs in the last few years for the treatment of metastatic breast cancer, including angiogenesis and aromatase inhibitors, specific receptor blocking agents, and cytotoxic treatments (*10*). Unfortunately, there has been a minimal effect from these therapeutic strategies on the overall survival and quality of life for patients with metastatic breast cancer (*11*)

Prostate, lung and colorectal cancer continue to be the most prevalent cancers among men (*6*). In the case of prostate cancer, the curability is 100% if the primary tumor is locally or regionally confined; however, the 5-year survival rate drops considerably when a patient is diagnosed with bone metastases (*12*). Table 1 shows bone metastases incidence for various cancer types. This difference in survival is a remainder that metastases are the true culprit.

Recently, ^{223}RaCl (Xofigo®), a new alpha-particle-emitting targeted-radionuclide-therapy agent, was approved by the FDA for the treatment of bone metastases in castration-resistant prostate cancer (CRPC). Patients have seen excellent results, providing palliative care and a significant increase in median survival from 11.2 to 14 months (*13*). The effectiveness of the treatment relies on the ability of high-LET (linear energy transfer) alpha particles from ^{223}Ra decay chain to kill cancer cells. Radium is favorably absorbed by bone by virtue of its chemical similarity to calcium creating a regional site of irradiation (*14*). The marginal increase in median survival is due to the fact that patients tend to suffer from other metastatic sites where ^{223}RaCl is totally ineffective (*13*). Most patients in late stages of metastatic prostate cancer are found to have involvement in bone (90%), lung (46%), liver (25%), pleura (21%), and adrenals (13%) (*15*).

Table 1. Bone metastases incidence among various cancers.

	Tumor	**Disease prevalence in the US ($\times 10^3$)**	**Incidence of tumor bone disease (%)**	**Median survival after diagnosis of bone metastases (months)**
Osteolytic	Myeloma	75-100	70-95	24
	Renal	198	20-25	12
	Melanoma	467	14-45	6
	Bladder	582	40	6-9
	Thyroid	207	60	48
	Lung	386	30-40	7
	Breast	1,993	65-75	24
Osteoblastic	Prostate	984	65-75	36

Like prostate cancer, malignant melanoma can be completely removed and cured through surgical resection. However, if the cancer metastasizes, it is one of the most aggressive and drug-resistant cancers with a very poor overall survival. Malignant melanoma is known to metastasize to all organs of the human body with a high incidence to the lungs and liver. The median survival of metastatic malignant melanoma is between 6 and 9 months (*16*).

It is important to understand how cancer metastases can be managed and treated. Based on the results obtained from the clinical trials carried out with the high-LET alpha-particle targeted-radionuclide-therapy compound ^{223}RaCl (Xofigo®), as well as other studies using ^{211}At and ^{125}I, *(3-6)* it seems metastases can be managed. High-LET targeted-radionuclide-therapy combined with advanced drug delivery systems based on nanotechnologies could provide organ-specific treatment strategies that could seek and destroy the early culprits of cancer metastases. This novel treatment has the potential to treat cancer metastases since nanoparticles are on the nanoscale, and can interact specifically with strands of DNA (*17*).

1.2 Circulating Tumor Cells and Micro-metastases

The concept of circulating tumor cells (CTC) was established as early as 1965 by Fisher and Fisher for liver metastases (*18*) and 1969 by Ketchman *et al.*, for pulmonary metastases (*19, 20*). The discovery of CTC and their prognostic capacity to forecast cancer metastases has opened a new opportunity for the management of patients. Circulating tumors cells have been shown to predict cancer metastases in prostrate (*21-*

23), breast (*24*), lung (*25-29*), melanoma (*16, 30-33*), sarcomas and osteosarcomas (*34-36*), bladder (*37-41*), and colorectal cancer (*42-56*). As for the case of breast cancer, although primary tumors are diagnosed at an earlier stage, many women will have CTC and sub-clinical micro-metastases (MM) in other organs at the time the primary tumor is surgically removed. From examinations at time of autopsy, 62% will have bone metastases, 66% will have lung metastases, and between 40% and 60% will have liver metastases (*57, 58*). Table 1 shows the incidence of bone metastases for different cancers.

Detection of CTC from peripheral blood samples, commonly referred as liquid biopsy, has been an area of extensive research. There are many commercial systems approved by the FDA capable of enriching, purifying and analyzing CTC from many primary tumor types. The CellSearch® system was used to carry out several pivotal studies. A study was carried out for breast cancer patients (n = 177) with no clinical symptom of metastases (*59*). Blood samples from these patients were obtained (7.5 ml), and they were divided into two groups, those with CTC < 5 (n = 90) and the other with CTC ≥ 5 (n = 87) per sample. The results indicated that the median progression free survival for those patients with CTC < 5 was 7.0 months and 2.7 months for those with CTC ≥ 5 with a log-rank P value of 0.0001. Progressive disease among patients within 3 months was 20% for CTC < 5 and 54% for CTC ≥ 5 with a Fisher's exact P value of < 0.001 (*59*). For the case of prostate cancer, CTC were able to predict the overall survival benefit for treatment of castration-resistant metastatic prostate cancer (CRPC) (*60*). The

overall median survival for those with CTC < 5 was 21.7 months versus 11.5 months for those CTC ≥ 5 with a P value of < 0.0001.

1.3 Current Treatment Strategies

Micro-metastatic disease is not clinically discernable by radiographic means and therefore a systemic treatment is needed irrespective of target organ (*61*). There are multiple treatment options for treating metastases; however, these treatments depend on target organ. Targeted therapies using biological agents have been used to treat metastases in the past (*62*).

Table 2. Physical characteristics of radiopharmaceuticals for palliative care (*63*).

Radionuclide	**Carrier**	**Physical half-life, days**	**β_{max} (MeV)**	**β_{mean} (MeV)**	**Mean range in tissue (mm)**	**γ energy (keV) (%)**
^{89}Sr	Chloride	50.5	1.46	0.583	6.7	-
^{153}Sm	EDTMP	1.95	0.8	0.224	3.4	103(28)
^{32}P	Phosphate	14.28	1.71	0.695	7.9	-
^{188}Re	HEDP	0.71	2.12	0.76	11.0	155(1)
^{117}Sn	DTPA	13.6	NA	NA	0.3	CE 159
^{33}P	Phosphate	25.34	0.249	0.85	0.05	-
^{223}Ra	Chloride	11.4	α-emitter (eff. energy 26.4 MeV)		< 100 μm	-

For bone metastases, treatment consists of bisphosphonates and low energy beta-emitting radionuclides conjugated with bone-seeking compounds such as ^{89}Sr, ^{153}Sm-ethylenediaminetetramethylenephosphonate, and the alpha-emitting radionuclide ^{223}RaCl

(Xofigo ®). Table 2 presents the physical characteristics of the radionuclides used in the treatment of bone pain.

The radionuclides mentioned in Table 2 are selected because of their physical properties, but most importantly because they do not need to be internalized into the cell to produce a cytotoxic effect. The range in tissue of the emitted beta and alpha particles are few to hundreds of cell diameters. However, cytotoxicity of these radiative emissions depends on their LET. The LET of beta particles is about 0.2 keV μm^{-1} and 100-200 keV μm^{-1} for alpha particles. The cytotoxic effectiveness of low LET particles and high LET particles is given in Figure 1 from the Linear Quadratic Model (LQM) for cell survival.

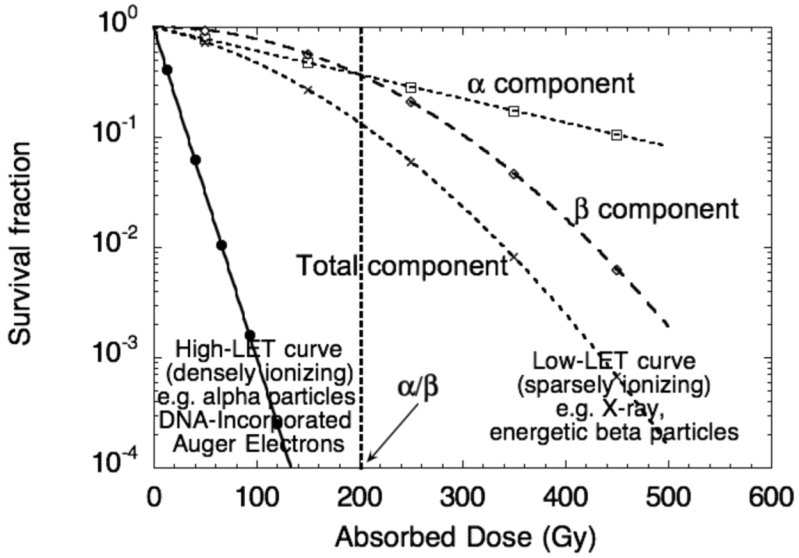

Figure 1. Survival fraction for different types of LET radiations. The LET is based on the Linear Quadratic Model (LQM). These absorbed doses are broken into their alpha, beta, and gamma components with LET shown.

LET is one of the physical characteristics of radionuclides examined in therapy, as each radiation type has its own specific LET. The LET is defined as the amount of energy deposited in the material the particle is traversing per unit length. Figure 2 shows the representation of this.

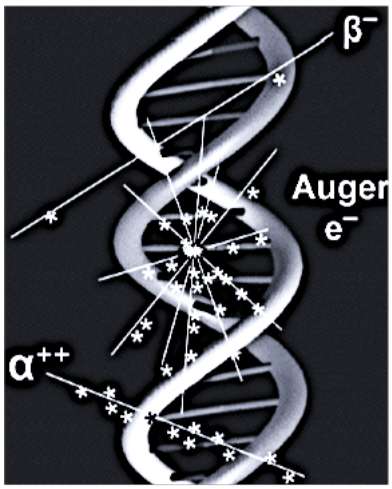

Figure 2. Energy deposition patterns for α, β, and Auger particles. Adapted from (*64*).

From Figure 2, it can be seen how the LET varies from particle to particle. The beta particles have a relatively low LET, while the alpha particles have a very high LET. Auger electrons also have a very low LET, however, when an Auger cascade occurs the combined energy deposition of these electrons results in a localized energy deposition that resembles high LET particles, such as an alpha particle (*65*). This phenomenon is taken advantage of in this project, as the radionuclides chosen are Auger emitters.

1.4 Future Treatment Strategies Targeting Circulating Tumor Cells and Micro-metastases Using Nanotechnologies

New systemic treatment strategies must be developed to target micro-metastatic disease at its early stages, including CTC. The treatment of MM and CTCs requires that therapies be localized or specific and effective on first "contact", requiring no significant cumulative dose of a drug to induce a cytotoxic effect. These specific demands require that new therapies be binary in their mode of action. Unfortunately most of the cytotoxic drugs mentioned above have a non-specific distribution, a negative pharmacokinetic profile, and lack specificity. Thus, the development of compartmental or multicomponent, multi-modal nanoparticle-based drugs for the specific delivery of cytotoxic drugs to tumor cells is a favorable strategy. In here several examples are presented using surface receptors, cell penetrating peptides, and inhibitors in combination with nanoparticles for the treatment of CTC and MM.

Cell surface receptors can be used as tagging agents. As an example, Peiris *et al*., (*66*) developed a flexible multi-chain nanoparticle system for the treatment of breast MM in an animal model. The multi-chain nanoparticle used a tripeptide to target the $\alpha_v\beta_3$ integrin receptor on the cell surface of metastatic breast cancer cells. The nanodrug was able to gain access to and be deposited at MM sites. Using a radiofrequency triggering system, the cytotoxic cargo was released into these cancer cells. The results are very promising as the system was binary and its cytotoxic effect was confined to those regions where the nanodrug accumulated.

Cell penetrating peptides (CPP) are used to bypass the lipophilic wall of cell membranes efficiently, and deliver a variety of agents. These peptides are capable of

introducing proteins, other peptides, and nanoparticles into the cell and its compartments. The CPP are basic, and rich in lysine- or arginine-, as well as being hydrophilic and lipophilic (*67*). CPP work in two different ways, by covalently linking to their cargo molecules, or by forming a complex with them. While CPP have great potential for drug delivery systems, they are still being investigated, as they penetrate almost all cell types non-specifically.

Inhibitor loaded dextran-based polymeric nanoparticles have been used to treat metastatic osteosarcoma, where the slow release or dissociation of the nanoparticle within the confinement of the tumor site was able to deliver an inhibitor and suppress tumor growth and proliferation (*68*).

Nanotechnology can be combined with radiation to effectively treat tumor cells through the delivery of radioactive atoms contained within nanoparticles that subsequently deposit energy in the cluster of tumor cells (*69-73*). Radioactive nanoparticles can be synthesized in two ways. The radioactive atoms can be integrated into the core or at the nanoparticle surface. The nanoparticle is then coated with specific biological agents for targeting purposes. This allows the nanoparticles to be administered to the patient and travel to the specified location and attach, or even penetrate, lesions or single tumor cells. The simplest method for manufacturing a radioactive nanoparticle is based on the synthesis of gold nanoparticles using the modified Turkevich method (*74*) with ^{198}Au (*69, 75*). This radioactive gold-in-gold approach is simple and requires no alloy formation. Radioactive ^{198}Au-AuNPs have been studied in preclinical animal models for treating prostate cancer (*69, 76*) and have been combined with

chemotherapeutics (*77*). These nanoparticles have been used for the treatment of localized breast cancer therapy after lumpectomy using radioactive liposomes loaded ^{186}Re and ^{188}Re radionuclides (*78*).

The spontaneous alloying of tin atoms into gold nanoparticles has been studied by Yasuda *et al*., (*79, 80*). The generation of Au-Sn alloy or AuSn compound nanoparticles has been carried out. It is possible to spike gold nanoparticles with ^{117m}Sn radioactive atoms to generate ^{117m}Sn-AuNP as an alloy or as an amorphous nanocluster.

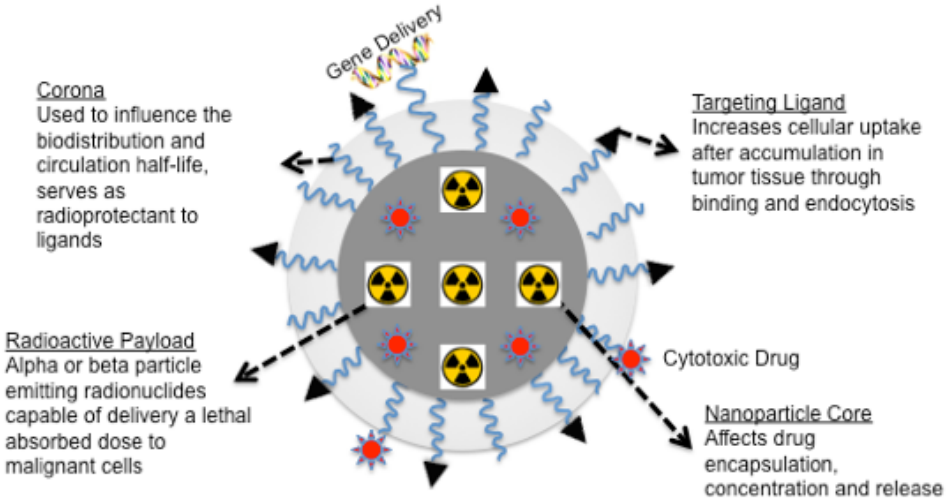

Figure 3. Schematic of a nanoparticle containing radioactive atoms. Examples include ^{125}I, ^{17m}Sn, or ^{211}At. The nanoparticle is PEGylated for stability and its surface coated or "functionalized" with various substrates targeting different cell receptors, such as monoclonal antibodies, fragments, peptides, and cell penetrating peptides.

Similarly, the generation of Gold(I)Iodide nanoparticles has been studied by Daniel and Astruc (*81*), showing that iodine surface absorption was possible by displacing citrate ions from AuNPs, leading to superstructures that are formed upon

addition of KI (*82*). These studies show that it is possible to construct radioactive gold nanoparticles in the form of amorphous or alloy clusters.

However, radioactive nanoparticles must be modeled to assess the energy deposition patterns and effects to the various structures they surround. These include the enhanced production of radical species within the immediate environment of the nanoparticle (*83-85*). Figure 3 is a representation of such a nanoparticle. Meisel *et al*., studied the charge or electron transfer in colloidal gold nanoparticles and its potential application and effects in radical production (*84-86*). It has been postulated that radical production by gold nanoparticles is enhanced, potentially increasing it cytotoxic effect. This is relevant when radioactive decay occurs within the core of the nanoparticle producing electron-hole pairs that travel through the nanoparticle and potentially escape from it, producing radical species.

1.5 Summary

The treatment of MM and CTC will require the development of multi-step combinatorial treatment strategies attacking different spatiotemporal targets during the cancer metastatic process. Single drug options, even single nanotechnology-based therapies, will not be able to tackle the different stages of metastatic evolution. The need to elucidate how metastases spread in pathophysiological and molecular terms is then fundamental for developing new strategies.

An analysis of the dosimetry of the potential utility of Auger electron emitters is presented. As indicated below, the Auger electron emitting radionuclides ^{125}I and ^{117m}Sn could be powerful killers when introduced into the cell nucleus (*87-91*).

2. METHODS AND MATERIALS

The simulation of the energy deposition of a single radioactive decay of a radionuclide from a nanoparticle requires the use of Monte Carlo methods capable of tracking the energy deposition pattern at the nanoscale level. Therefore, the present project needs to be divided into multiple parts. The first part is to understand the radioactive decay of the radionuclides ^{125}I and ^{117m}Sn, and the particle emitted through a single decay. The second part is to carry out the simulation of the particle transport through water and calculate the energy deposition patterns around the nanoparticle. In the current work absorbed dose will not be calculated, as absorbed dose loses any meaning at the nanoscale level where direct and indirect effects are of relevance. The third part is the conceptual propagation of effects from physical to physicochemical, chemical, and finally to biological effects with an emphasis on probability of superimposition. The fourth part is the development of the mathematical framework for the spatiotemporal decay of multiple radioactive atoms under the principle of superimposition.

2.1 Auger-Emitting Radionuclides

More than half of the radionuclides known decay by internal conversion and/or electron capture resulting in the emission of a cascade of extremely low energy electrons, a phenomenon commonly known as the Auger effect (*92*). These Auger, Coster-Kronig and super Coster-Kronig electrons typically have energies between few eV and 1 keV. These electrons travel short distances, up to ~ 1000 nm from the decay

site and deposit all of their energy in a small spherical volume with a radius of approximately 2000 nm. The relative biological effectiveness (RBE) of Auger electrons was initially ignored owing to their low electron energy. However, after observing in cell survival studies the lack of a shoulder (*91*), Auger electrons are considered extremely cytotoxic as they emulate high-LET radiation (2–25 keV/μm) imparting very high cytotoxicity to mammalian cells when the decay site is located in close proximity to the nuclear DNA (*93, 94*). These observations drove much of the interest in therapeutic potential of Auger electrons (*95*).

2.1.1 Radionuclide ^{125}I

One of the most studied and used radionuclides in medicine is ^{125}I. It has a physical half-life of 59.4 d. It decays by electron capture (100% EC) into ^{125m}Te ($t_{1/2}$ = 1.6×10^{-9} s), and then into stable ^{125}Te. The neutron-based production of ^{125}I is based on the reactions

$$^{124}\text{Xe}(n,\gamma)\rightarrow{}^{125m}\text{Xe}(57\text{ s})\rightarrow{}^{125}\text{I}\ (59.4\text{ d})$$

and

$$^{124}\text{Xe}(n,\gamma)\rightarrow{}^{125g}\text{Xe}(19.9\text{ h})\rightarrow{}^{125}\text{I}\ (59.4\text{ d})$$

using natural xenon in a zirconium canister at about 100 atm. ^{125}I has a variety of uses, mainly in the realm of radioimmunoassay, brachytherapy and targeted radionuclide therapy (*91, 96*). ^{125}I is preferred for low dose rate brachytherapy treatments because the photons emitted have low energies (*97*). Since they are low energy and have a short range, brachytherapy seeds can be used to deliver a localized dose to treat specific sites

in the body. Along with the low energy photons, Auger electrons are also emitted. The Auger electron cascade affects a very small volume, because they have a very short range, on the order of few hundred nanometers (*89*). Both of these physical attributes are ideal, due to the fact that a large burst of energy can be deposited almost precisely where needed. Even though the Auger electrons have very low energy, they can cause serious biological damage as they produce a cluster of ionization simulating a high-LET event; thus, it can produce significant effects to sensitive targets, such as DNA.

Within the iodine family, there are other radionuclides apart from ^{125}I used in medicine. These include ^{123}I ($t_{1/2}$ = 13.13 h) and ^{124}I ($t_{1/2}$ = 4.18 d), and ^{131}I ($t_{1/2}$ = 8.019 d). The radionuclide ^{123}I is mostly used in diagnostic nuclear medicine. It is preferentially selected for nuclear imaging scans when dealing with the thyroid, since the thyroid readily uptakes iodine. The photons emitted from this isotope are ideal for diagnostics involving gamma cameras and SPECT (*98*). The radionuclide ^{124}I is primarily used as a radiotracer in positron emission tomography (PET). This isotope has a long half-life and is known to be optimal for PET scanning, due to the way it can help directly image the thyroid (*99*). The last isotope of iodine used in nuclear medicine is ^{131}I. This isotope emits both photons and betas, making it suited for both diagnostics and therapy. It can be used in SPECT imaging, but is more commonly used for its therapeutic purposes for the therapy of differentiated thyroid carcinoma (*100*).

The decay scheme for ^{125}I is shown in Figure 4, obtained from the National Nuclear Data Center (NNDC).

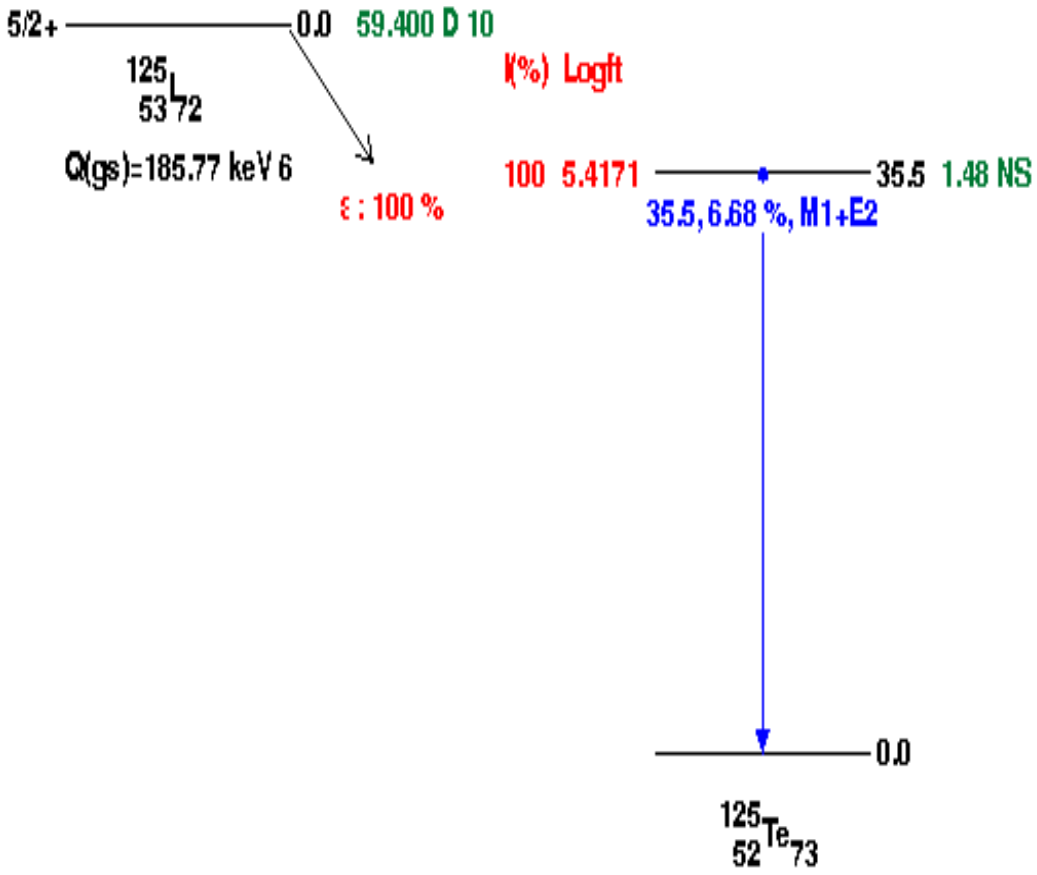

Figure 4. Decay scheme of ^{125}I. Adapted from the NNDC.

The decay scheme of ^{125}I contains conversion electrons and photons emitted from this radionuclide during decay. A more detailed report of the radiations emitted during the decay of ^{125}I is shown in Table 3.

Table 3. Radiative emission, yields, and energies for ^{125}I in MIRD format. Obtained from the NNDC.

^{125}I

Half-life = 59.400 Days
Decay Mode: EC
February 2011

Radiations	y(i) $(Bq\text{-}s)^{-1}$	E(i) (MeV)	y(i) ×E(i) (MeV)
γ 1	6.68×10^{-02}	3.549×10^{-02}	2.37×10^{-03}
ce-K, γ 1	7.81×10^{-01}	3.679×10^{-03}	2.87×10^{-03}
ce-L, γ 1	1.07×10^{-01}	3.055×10^{-02} a	3.26×10^{-03}
ce-M, γ 1	2.13×10^{-02}	3.449×10^{-02} a	7.35×10^{-04}
ce-N+, γ 1	4.66×10^{-03}	3.532×10^{-02} a	1.64×10^{-04}
Kα1 X-ray	7.35×10^{-01}	2.747×10^{-02}	2.02×10^{-02}
Kα2 X-ray	3.94×10^{-01}	2.720×10^{-02}	1.07×10^{-02}
Kβ X-ray	2.56×10^{-01}	3.100×10^{-02} *	7.93×10^{-03}
L X-ray	1.48×10^{-01}	3.770×10^{-03} *	5.57×10^{-04}
Auger-K	1.97×10^{-01}	2.270×10^{-02} *	4.47×10^{-03}
Auger-L	1.57	3.190×10^{-03} *	5.00×10^{-03}
Listed X, γ, and $\gamma^{\pm}$ Radiations			4.18×10^{-02}
Listed β, ce, and Auger Radiations			1.65×10^{-02}
Listed Radiations			5.83×10^{-02}
* Average Energy (MeV)			
[a] Maximum Energy (MeV) for subshell			
Tellurium-125 Daughter is stable			

The decay of ^{125}I into ^{125m}Te and then into ^{125}Te produces a series of primary electronic vacancies. The probabilities of these vacancies were calculated using Monte Carlo methods by Charlton and Booz and they are shown in Table 4 (*101*).

Table 4. Primary vacancy yields after EC and IC of ^{125}I decay.

Atomic Shell	EC to ^{125m}Te	IC from ^{125m}Te
K	0.808	0.795
L_1	0.154	0.095
L_2	0.004	0.007
L_3	-	0.004
M_1	0.035	0.019
M_2	0.001	0.004
M_3	-	0.001
M_{4-5}	-	-
N_1	-	0.004
N_2	-	0.001
Total	1.000	0.930

2.1.2 Radionuclide ^{177m}Sn

The radionuclide ^{177m}Sn ($t_{1/2}$ = 13.76 d) is particularly new in the medical field, and has recently been used for its ability to treat painful bone metastasis (*102*). However, it has many of the same physical properties of ^{125}I, including Auger electron emissions. ^{117m}Sn is produced in a cyclotron using a highly enriched cadmium target of ^{116}Cd (99%) via ^{116}Cd(α,3n)^{117m}Sn with an alpha particle beam of 35 MeV, a minimum beam current of 5 μA and a 10° slope to the target surface. ^{117m}Sn is chemically separated and the target is recycled (*103*).

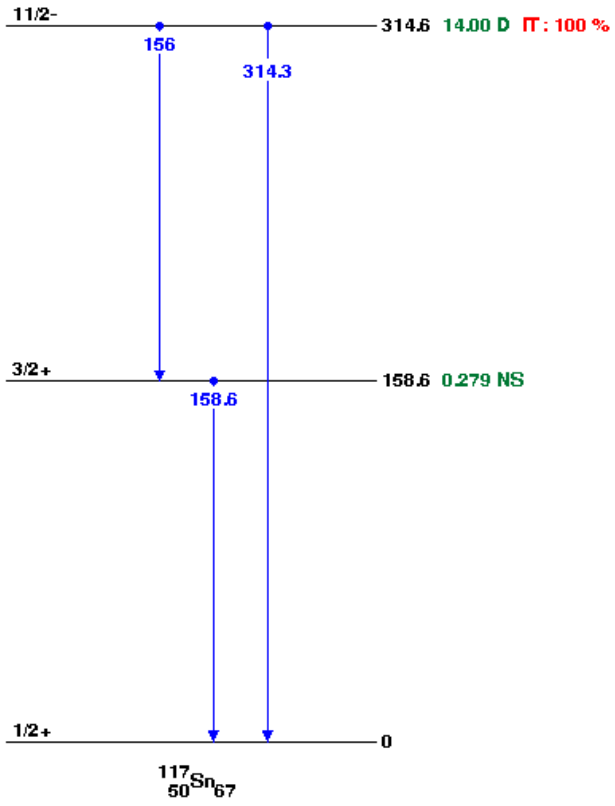

Figure 5. Decay scheme of ^{117m}Sn. Adapted from the NNDC.

The decay scheme of ^{117m}Sn is shown in Figure 5, with decay occurring through isomeric transition. A more detailed report of the radiations emitted during the decay of ^{117m}Sn is shown in Table 5.

Table 5. Radiative emission, yields, and energies for ^{117m}Sn in MIRD format. Obtained from the NNDC.

^{117m}Sn

Half-life = 14.00 Days
E (excitation) = 0.3146 MeV
Decay Mode: IT
January 2011

Radiations	y(i) $(Bq\text{-}s)^{-1}$	E(i) (MeV)	y(i)×E(i) (MeV)
γ 1	2.11×10^{-02}	1.560×10^{-01}	3.30×10^{-03}
ce-K, γ 1	6.57×10^{-01}	1.268×10^{-01}	8.34×10^{-02}
ce-L, γ 1	2.65×10^{-01}	1.516×10^{-01} a	4.02×10^{-02}
ce-M, γ 1	5.79×10^{-02}	1.551×10^{-01} a	8.98×10^{-03}
ce-N+, γ 1	1.11×10^{-02}	1.559×10^{-01} a	1.73×10^{-03}
γ 2	8.64×10^{-01}	1.586×10^{-01}	1.37×10^{-01}
ce-K, γ 2	1.13×10^{-01}	1.294×10^{-01}	1.46×10^{-02}
ce-L, γ 2	1.56×10^{-02}	1.541×10^{-01} a	2.40×10^{-03}
ce-M, γ 2	2.89×10^{-03}	1.577×10^{-01} a	4.55×10^{-04}
ce-N+, γ 2	5.89×10^{-04}	1.584×10^{-01} a	9.34×10^{-05}
γ 3	4.23×10^{-06}	3.143×10^{-01}	1.33×10^{-06}
ce-K, γ 3	4.05×10^{-06}	2.851×10^{-01}	1.15×10^{-06}
ce-L, γ 3	2.68×10^{-06}	3.098×10^{-01} a	8.30×10^{-07}
ce-M, γ 3	5.74×10^{-07}	3.134×10^{-01} a	1.80×10^{-07}
ce-N+, γ 3	1.05×10^{-07}	3.142×10^{-01} a	3.31×10^{-08}
Kα1 X-ray	3.54×10^{-01}	2.527×10^{-02}	8.94×10^{-03}
Kα2 X-ray	1.89×10^{-01}	2.504×10^{-02}	4.74×10^{-03}
Kβ X-ray	1.20×10^{-01}	2.850×10^{-02} *	3.41×10^{-03}
L X-ray	7.41×10^{-02}	3.440×10^{-03} *	2.55×10^{-04}
Auger-K	1.08×10^{-01}	2.100×10^{-02} *	2.26×10^{-03}
Auger-L	9.27×10^{-01}	2.950×10^{-03} *	2.73×10^{-03}
Listed X, γ, and $\gamma^{\pm}$ Radiations			1.58×10^{-01}
Listed β, ce, and Auger Radiations			1.57×10^{-01}
Listed Radiations			3.14×10^{-01}

* Average Energy (MeV)
[a] Maximum Energy (MeV) for subshell
Tin-117 Daughter is stable

2.1.3 Energy Range of Auger Electrons in Liquid Water

Auger electrons have a plethora of energies as indicated above and their range in water varies accordingly. The penetration of low energy electrons in water has been studied by Meesungnoen, *et. al.* Figure 6 shows these values, calculated using Monte Carlos and theoretical methods.

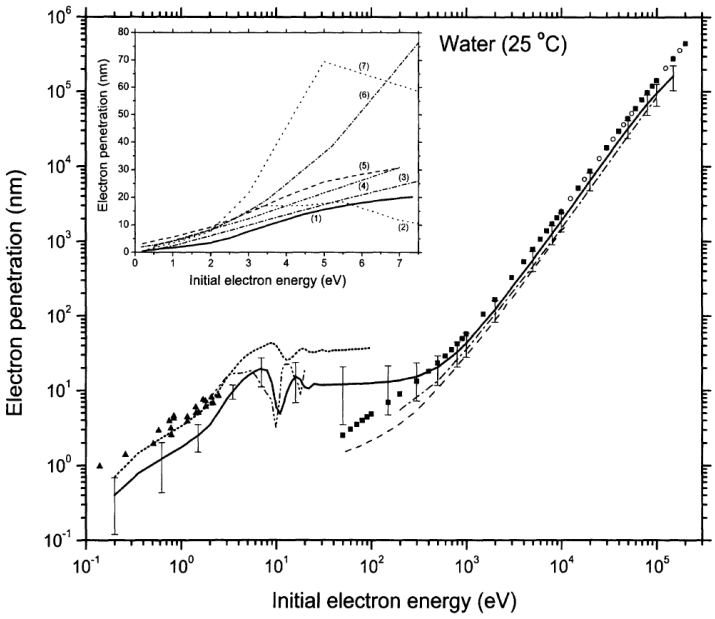

Figure 6. Electron penetration as a function of initial electron energy. Adapted from (*104*).

The Auger electrons emitted from the radionuclides have a very specific range to travel and deposit their energy. This is the basis of this work, and must be very well understood. The electron ranges for ^{125}I and ^{117m}Sn are shown in Table 6.

Table 6. Electron range based on specific Auger electron energies. Adapted from (*104, 105*).

Radionuclide	Radiation	Average Energy (MeV)	Yield	Penetration Range (nm)
^{125}I	Auger-K	2.270×10^{-02}	1.97×10^{-01}	14000
^{125}I	Auger-L	3.190×10^{-03}	1.57	420
^{117m}Sn	Auger-K	2.100×10^{-02}	1.08×10^{-01}	7000
^{117m}Sn	Auger-L	2.950×10^{-03}	9.27×10^{-01}	250

2.1.4 Energy Range of Low Energy Electrons in Matter

For low energy electrons below 5 keV the usual Bethe-Bloch formula is inadequate for calculating the energy loss per unit path length; therefore, for low energy electrons a complex dielectric function is required to calculate the energy response of the material to a given energy transfer and momentum transfer. The dielectric function is determined solely by material properties, and how light traverses through the material (*106*). In a relatively constant field this variable describes to what degree a material will concentrate electric flux. This formalism is then used to calculate the continuous slowing down approximation (CSDA) range is given as

$$R_0(E) = \int_{10\ \mathrm{eV}}^{E} \frac{dE'}{S(E')}, \tag{1}$$

where $S(E)$ is the electron stopping power, which has been calculated for many materials, including gold (*107, 108*). The CSDA ranges from 15 eV to 6 keV are shown in Figure 7 for polystyrene, collodion, silicon, and gold. However, it is indicated that these estimates can be used with confidence down to 100 eV and errors up to 100% can be expected for energies at 10 eV. Nevertheless, these energy-range calculations are

suitable for our modeling purposes. The energy-range relationship will be used to estimate the energy of Auger electrons that will be stopping within the gold nanoparticle.

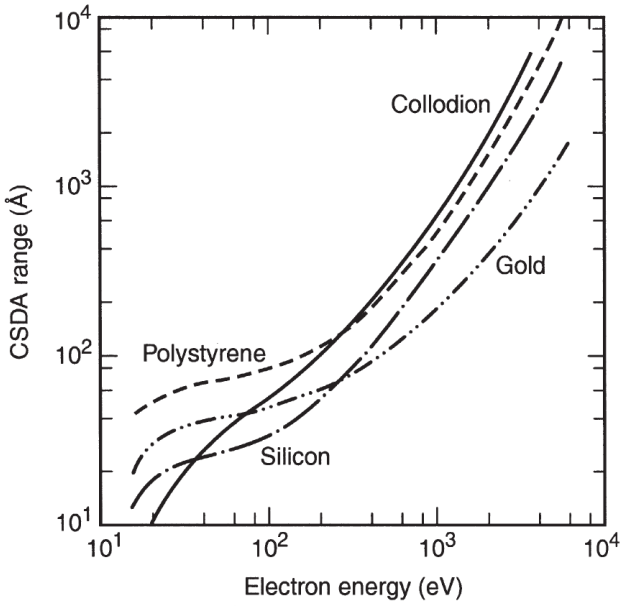

Figure 7. CSDA range for electron energies between 15 eV to 6 keV.

2.2 The Time Scale of Effects in Radiobiology

In radiobiology, there are three phases typically considered when radiation interacts with matter. These phases are a) physical, b) chemical, c) physiochemical, and d) biological. The time scale for each process is given in Figure 8.

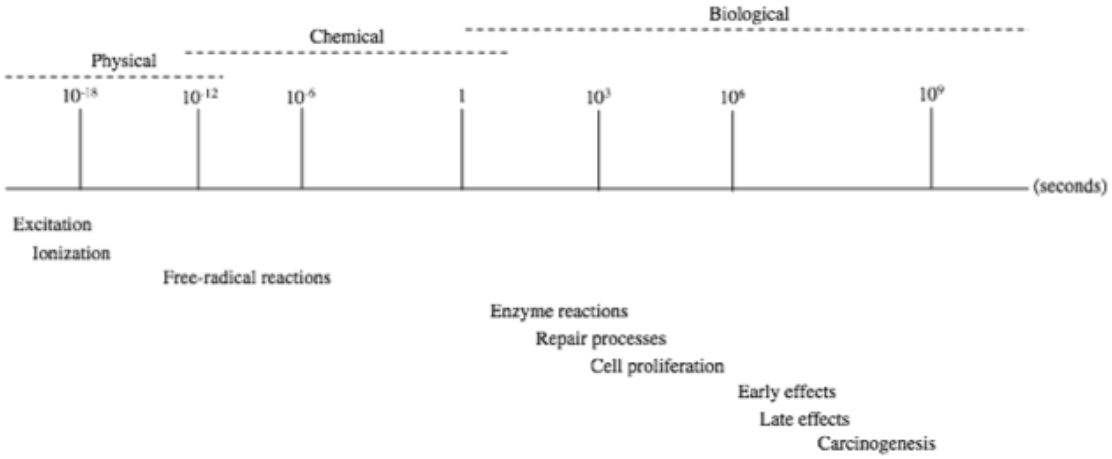

Figure 8. Time scale and events of radiation biology. Adapted from (*109*).

2.2.1 Energy Deposition

The first step is direct action, where particles interact with matter directly, physically damaging DNA by breaking bonds. This is referred to as the physical process, and its typical duration is 10^{-16} s (*109*).

2.2.2 Radical Generation

The next stage is the physiochemical stage, an in between stage where the physical processes are ending and the beginnings of the chemical stage are occurring. This process lasts for about 10^{-12} s. The chemical stage is next, continuing for about 10^{-6} s. In it, the particles from radioactive decay are no longer directly damaging the DNA, but have produced secondary particles are free radicals through excitation and ionization that go on to damage the DNA. Figure 9 shows the radiolysis of water, and the radicals generated from it.

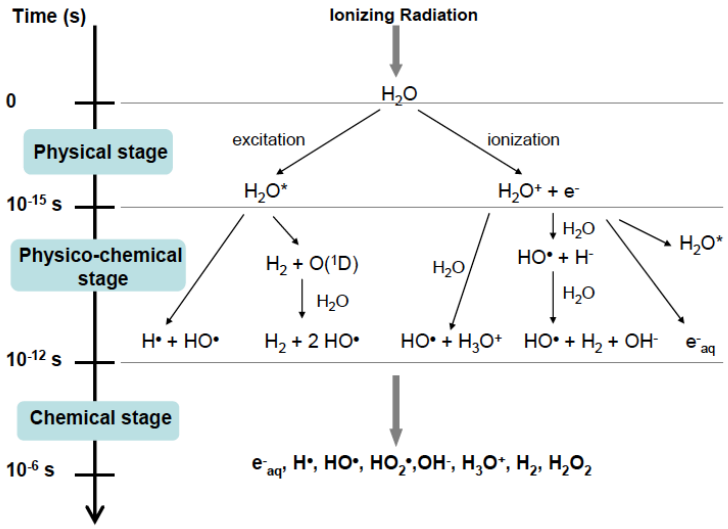

Figure 9. Products from the radiolysis of water. Adapted from Le Caër (*110*).

It is important to model indirect effects, as they also contribute to DNA damage. The radicals are produced via secondary electron interactions with molecules other than the actual DNA, such as water within the cells. When these energetic electrons interact with water, for example, radicals such as hydroxyls are produced (*111*). These radicals then go on to damage the DNA themselves. For this model κ will be used as the variable to describe the number of radicals generated.

$$G_{H_2O} \rightarrow G_{H^\bullet} + G_{e^-_{aq}} + G_{H^+} + G_{^\bullet OH} + G_{H_2} + G_{H_2O_2}, \tag{2}$$

where:

$G_{H^\bullet}$ is the number of hydrogen radicals produced

$G_{e^-_{aq}}$ is the number of hydrated electrons produced

$G_{^\bullet OH}$ is the number of hydroxyl radicals produced

G_{H_2} is the number of hydrogen atoms produced

$G_{H_2O_2}$ is the number of hydrogen peroxide atoms produced

The variables above represent the radical products that will be present at the beginning of the chemical phase (*112*). However, the G-values are dependent upon the type of radiation interacting with the water (*110*). Thus, the radicals produced by the Auger electrons during the decay of ^{125}I or ^{117m}Sn are clustered and therefore may be different than those produced by sparse radiations from photons produced by ^{60}Co or ^{137}Cs. The G-values for various radicals from irradiation of neutral water with a ^{60}Co source are listed in Table 7.

Table 7. G-values for various radical species.
Adapted from Meesungoen, *et. al.* (*112*)

Variable	Yields (molecules/100 eV)
$G_{H\cdot}$	0.60
$G_{e^-_{aq}}$	2.65
$G_{\cdot OH}$	2.80
G_{H_2}	0.45
$G_{H_2O_2}$	0.68
G_{-H_2O}	4.14

The spatiotemporal evolution of the chemical species from electrons in pure water has been studied using Monte Carlo methods by Terrisol and Beaudré (*113*). They showed that the G values for the production of different species for a 10 keV electron changed considerably as a function of time. The radical generations can be seen in Figure 10.

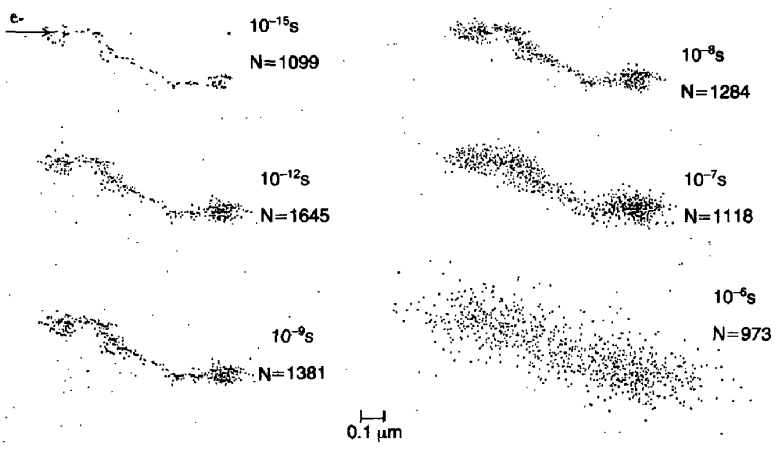

Figure 10. Spatiotemporal development of chemical species. The species was generated by one 10 keV electron track in liquid water. Each dot represents one species and N is the number of molecules present at the time considered. Adapted from (*113*).

2.2.3 Biological Effects

The last step is the biological phase, in which the damage takes effect and consequences can be seen. This stage lasts anywhere from minutes to hours to weeks to years. For these calculations, it was assumed to be 10^6 s. The biological phase can last up to years, when late effects and carcinogenesis become prevalent. However, early effects are seen sooner, from days to weeks. Due to this, 10^6 s was chosen.

It is extremely important to assess radical production in modeling the energy deposition from gold nanoparticles since it is a major indirect effect and plays a large role in DNA damage. In this model, it will be represented by ζ.

The Auger electron spectrum of the radionuclide ^{125}I is well studied and for its, subsequent direct effects (*114*). However, if the radioactive iodine molecule is at a distance longer than a few nanometers from DNA, where the direct effects cannot occur,

the radical production will surely arise. If this happens, it is imperative that the radical production be taken into account. The numbers of radicals produced needs to be known, and the energy deposition from them should be accounted for. These are both important to understand so the degree of damage to the DNA can be properly assessed.

The molecular changes can occur anywhere from seconds to hours after the initial radiation exposure (*111*). Molecular changes lead to DNA damage, such as single and double strand breaks and aberrations, and other early physiological effects. These effects are considered reversible, because the damage inflicted can usually be repaired (*115*). In repair, there are two general cases that can occur. The cell can repair itself and continue to function in a healthy manner, or the damage will not be repaired correctly, and mutations have the chance to occur cellular generations later. However, if the damage is too intense for the cell to repair, the cell may die by means of apoptosis, which is programmed cell death, or mitotic catastrophe (*111*). Repair to the cells are usually completed in a matter of hours, but mutations in the DNA, such as genetic damage and neoplastic transformations can persist for years (*115*).

There are several effects that can come from DNA damage, all in varying forms of severity. Some of the most common damages are single strand breaks that can easily be repaired. However, double strand breaks can also occur, which are more difficult to fix, and other aberrations such as dimers can occur (*111*). While these types of damage can be repaired, they take longer to fix and there is a higher chance of error occurring during the repair process, since the damage is more complicated.

2.2.4 Probability of Superimposition

For the simulations of the radioactive nanoparticles, each nanoparticle was assumed to contain one radioactive atom. This was done for theoretical purposes, so the energy deposition from a single decay could be analyzed. However, we must also look at the probabilities for multiple radioactive atoms contained within the nanoparticle. The Poisson distribution is followed for several reasons. This distribution calculates the probability that a certain event will occur within a specific time range, if the events are independent. Since radioactive decay is independent, the Poisson distribution is a perfect model.

$$P(x;\mu) = \frac{\mu^x e^{-\mu}}{x!} \tag{3}$$

In Equation (3), x represents the actual number of decays, μ is the expected number of decays, and $P(x;\ \mu)$ is the probability that exactly x number of decays happen when the expected number of decays is μ. The following equation was used to determine μ:

$$\mu = \Delta t \cdot \lambda \tag{4}$$

The calculation for the average number of decays occurring is shown in Equation 2. The variables that make up this equation are Δt, the duration of a process occurring, and λ, the decay constant of the radionuclide. Equation 2 only holds true when μ is much less than 1, which is satisfied in both cases.

With this information, the expected number of decays from Equation 2 can be calculated, which can then be used to find the Poisson distribution. The final calculations can be found in Table 8.

Table 8. Poisson probabilities of multiple decays occurring.

		Probability of Superimposition							
Process	**Time (sec)**	**x=0**		**x=1**		**x=2**		**x=3**	
		^{125}I	^{117m}Sn	^{125}I	^{117m}Sn	^{125}I	^{117m}Sn	^{125}I	^{117m}Sn
Physical	10^{-16}	0	0	0	0	0	0	0	0
Physiochemical	10^{-12}	0	0	0	0	0	0	0	0
Chemical	10^{-6}	0	0	0	0	0	0	0	0
Biological	10^{6}	0.874	0.558	0.118	0.325	0.008	0.095	0.000	0.0184

From Table 8, it can be seen that the probabilities only matter when looking at the biological effect. Therefore, new methods must be used to calculate energy deposition, such as Monte Carlo transport of ultra low energy electrons to account for a single decay. Other methods, such as point kernels, would be irrelevant on such a small time scale, and the results from such approaches would be skewed since they cannot be accurately calculated.

2.3 The Geant4-DNA Monte Carlo Transport Code

In the first phase of the project, Geant4-DNA was used to calculate the energy deposition from gold nanoparticles containing ^{125}I and ^{117m}Sn. In doing this, a complete understanding of the decay scheme of both radionuclides will be necessary, as well as a full understanding of the Auger electrons emitted from them. Once these schemes are

clear, Geant4-DNA was utilized to generate the energy deposition from these Auger electrons emitted in radioactive decay from ^{125}I or ^{117m}Sn to the DNA.

2.3.1 Geant4-DNA Overview

To simulate and model the energy deposition from the radioactive gold nanoparticles, Geant4-DNA was employed. This is an extension toolbox to the original Geant4 (GEometry ANd Tracking 4) code published CERN (*116*). This extension code was mainly created for radiobioligcal work, and is imperative in the field of micro and nanodosimetry. The Geant4-DNA architecture is based upon C++. The classes used in Geant4-DNA can be seen in Figure 11.

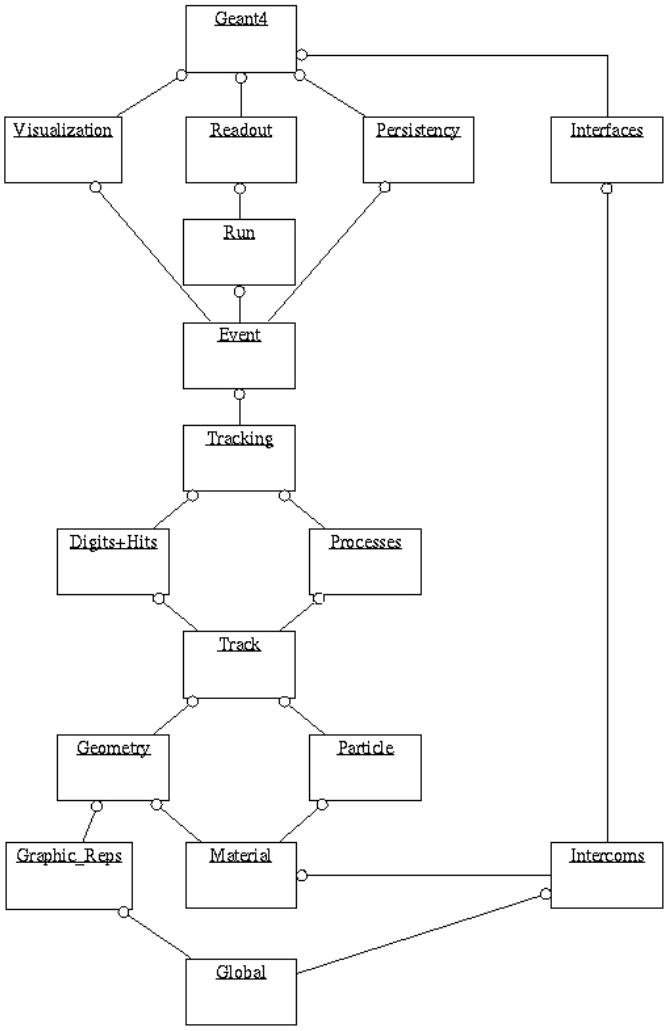

Figure 11. Geant4 class category diagram. Adapted from CERN.

The main physical processes are represented by classes, of which there are three types: discrete, continuous, and at-rest. Examples of these include Compton scattering, continuous electromagnetic energy loss, and at-rest disintegration, respectively. The process types can also be combined to form more complex interactions (*117, 118*).

2.3.2 Classical Trajectory Monte Carlo Methods

Geant4-DNA uses a Classical Trajectory Monte Carlo approach when dealing with paritcles. Ions and their trajectories are created under specific limits. The particle movement is characterized by Newtonian laws. The Classical Over-Barrier criteria is used to choose if a single or double ionization event will occur (*119*). The position of the binding energy of the target electron relative to the maximum of the Coulomb potential barrier that exists between the ion projectile and molecular barrier are connected. This method is used to track and simulate the proton interactions between hydrogen atoms from liquid water (*119*).

Monte Carlo codes have been relied upon as the basis of radiation transport calculations for some time, due to their ability to compute the absorbed dose to a macroscopic area or record the detailed track structure in a microscopic area. This is important because while the macroscopic codes sum up smaller events, on a molecular level these small events are the very basis of radiobiology, and have to be completely understood. With that, electrons formed in the process of radiation particles slowing down in matter are also of consequence to the DNA. This is because at this small of a range, in the nanometers, dose is simply too large of a parameter to calculate. Geant4-DNA is one of the first codes that allow particles to be tracked down to the energy of a few eV's, which subsequently allows for the radiation to be studied at the cellular and sub-cellular levels (*116*). This code can reproduce both direct and indirect effects on DNA when damaged by ionizing radiation, on both the cellular and molecular level. These biological effects can also be visualized with Geant4-DNA (*120*).

2.3.3 Track Structure Code in Geant4-DNA

Recently, there has been a greater need to simulate ionizing radiation on the cellular level so we are aware of radiobiological interactions occurring. Due to the stochastic nature of radiation, Monte Carlo codes are commonly used to calculate various parameters (*121*). General-purpose Monte Carlo codes that have been used in the past for these simulations are not able to give detailed tracking information required for radiobiological purposes. This is due to several factors. When working at the nanoscale level, discrete energy deposition cannot be treated as a binary process, as it is in general Monte Carlo methods (*122*). Usually, the electronic binding energies are magnitudes of order smaller compared to the discrete energy deposition previously mentioned, but this is not the case on the molecular scale, or when there are extremely low energies (*122*).

The solution to this is a "track structure" code, where some Monte Carlo techniques are taken into account, and energy deposition over the track length is recorded, along with where free radical species are produced. When Monte Carlo methods are used in track structures, the principle of superposition is generally used (*123*). This code transforms the way that tracking particles is done, primarily since it is able to track particles event-by-event and compile a detailed particle history, along with the secondary electrons (*124*). Large energy depositions also occur from secondary particles, so they too need to be tracked. All physical processes, either leading to energy deposition in the medium or directional changes, are taken into accunt to produce an extrememly detailed and precise particle history and track structures (*121*). Since the full particle history is available, essentially the damage on the cellular level, a better idea of

the damage to the DNA can be gained (*123*). One way this was accomplished was by reducing the volume and lowering the energy threshold that a general Monte Carlo code would work with (*124*).

With this, the Geant4 Monte Carlo simulation toolkit can mimic, event-by-event, the transportation of particle along with their successive particle cascade in liquid water or other mediums (*125*). This toolkit is extremely versatile, and can be changed readily to fit the user's needs. Parameters such as geometry, particle type/energy, run management, and energy range can be changed (*126*). The ability to change the radioactive decay model implemented and low-energy physics classes also makes it a valuable tool (*127*).

Geant4 can compute discrete interactions in the low energy range, if the appropriate corresponding low energy cross-sections are developed (*123*). Various papers have come up with their own way to do this, as well as employing the built-in Geant4 methods. Dealing specifically with electrons, it is important to be able to track them event-by-event. The electron slowing-down spectrum is the energy distribution of the electrons, when it satisfies the conditions of electronic equilibrium. Electronic equilibrium is fulfilled when the number of electrons that deposit their energy and stop moving is equal to the number of electrons set in motion. This information is needed in radiobiological work because it records the energy distribution of the electrons entering the cells (*128*). In Geant4, electrons can be tracked down to thermal energies, which occur around 0.025 eV (*124*). When electrons have reached these thermal energies, they can still be looked at in terms of vibrational excitations and dissociative attachments are

simulated (*121*). Specifically, vibrational excitation occurs from 2 eV to 100 eV, and electron attachment occurs from 4 eV to 13 eV (*123*). Excitation for electrons occurs starting at 9 eV, and ionization for electrons occurs beginning at 11 eV. Both of these processes go up to 1 MeV (*128*). The final position of the electron is also known, which is imperative in the radiobiological field. This is not only important to see where the final energy is deposited, but also for physiochemical and chemical stages, processes that will be available in later expansions (*121*).

2.3.4 Electron Processes

The four electron processes considered in Geant4-DNA include inelastic scattering, elastic scattering, which is modeled with the analytical Screened Rutherford model or Champion model, excitation, and ionization (*120, 129*). The former two are both interpolated. One method introduced to calculate the cross-sections for inelastic scattering included the Plane-Wave First Born Approximation following the dielectric formalism, for both ionization and excitation, and when it failed at very low energies they were based on semi-empirical models (*130*). When the electrons were in the low energy range, corrections were made using the exchange term from ICRU Report 37, along with a Coulomb field correction (*117, 118*). The classic Coulomb field correction is used to account for perturbation effects because it takes into account the potential energy gained by electrons in the field of the target molecule (*130*).

Elastic scattering occurs frequently with low energy electrons, and although energy is not lost, it is important to simulate. This was done using the screened

Rutherford and Champion models (*117, 118*). When the electrons go under 8 eV, the energy in the shell of the target material becomes too large, and the electrons cannot ionize it. However, vibration and rotation are still available, and phase-scaling procedures are used on experimental cross-sections of ice targets (*117, 118*). Electron dose point kernels were used to test the accuracy of Geant4-DNA models for low energy elastic and inelastic processes. While inconsistencies were found in other Monte Carlo codes, the results from Geant4-DNA were found to be consistent for electrons from 10 keV to 100 keV, when compared to the dose point kernel results (*131*).

2.3.5 Water Model in Geant4-DNA

The only medium available for use in Geant4-DNA is liquid water, due to the availability of approximate cross-sections. It is modeled in a very specific way, with an equal number of excitation and ionization shells. There are five excitation levels that are used. Each discrete energy transition has a specific total cross-section for excitation calculated for it, with correction factors applied at low energies (*122*). Tracks from primary events, as well as secondary events, are recorded here (*132*). This information can later be superimposed onto a DNA geometry model. In the physics list for electrons, ionization is also included, as mentioned above. The cross-sections used here are based on semi-empirical models, using the dielectric formalism for the valence shells and binary approximations for the K-shell (*122*). The dielectric formalism is used for both excitation and ionization for the K-shell models. It employed ICRU Report 55 and others for the correction factors (*117, 118*).

2.3.6 Geometrical Models of DNA

Apart from the need to track events and implement low energy physics, geometrical models are also needed. A model for B-DNA was created to use in conjunction with Geant4-DNA for ionizing radiaiton simulations. A variety of particles can be used with this geometric model, as long as the medium can be human genetic material. With this model, the chemical and radical species can also be viewed (*125*).

2.3.7 Physics Models used in Geant4-DNA

The cross-sections are also very important to consider when using Geant4, as they are directly tied into the interactions. The Binary-Encounter-Bethe and Deutsch-Mark models were used as the ionization cross-section models of choice. With these models, an ionization cross-section library was made that could possibly be implemented in future version of Geant4 (*133*).

One group looked into the hydroxyl radicals that cause damage to the DNA, modeling it with Geant4-DNA. Since the energy deposition must occur within a specific distance to cause damage, the spatial distribution of the ions located within simulation voxels were calculated with this tool. The ion coordinates on the nanoscale level were also generated. From this work, a first principles computational model was developed to study the interaction between ionizing radiation and the DNA molecules at the cellular level, which delved into the DNA damage occurring at the atomic level (*134*).

2.3.8 Gold Nanoparticle Models Used in Geant4-DNA

Geant4 was used to calculate energy deposition to DNA from radioactive atoms of ^{125}I or ^{117m}Sn housed within gold nanoparticles. Particle tracking was confined to 1000 nm, commonly referred to as the world in computational Monte Carlo transport. In order to visualize the energy deposition patterns, the code VisIt was used. The energy deposition (eV) patterns were stored for further analysis. In here the gold nanoparticle serves as a point of decay with no significant effect in energy deposition patterns outside of it.

The main purpose of this project is to calculate the potential damage to DNA from decays within a single nanoparticles. At the nanoscale level, energy is deposited in spatiotemporal terms where one decay cannot be superimposed over another. It is more important to be able to identify the energy deposition to certain structures within the cell, the most radiosensitive being the DNA. Another reason that energy deposition is calculated, and not the dose, is that a certain amount of information is available when the energy deposition is known. Factors such as the type of damage inflicted to the DNA, as well as the possible number of damages can both be found from this code, using energy deposition. Past experiments have shown how much energy is needed to induce specific types of damage to DNA, and from this code it was modeled. Other features that Geant4-DNA is capable of modeling include the formation of free radicals, and how they affect DNA. This is imperative to understand when modeling ionizing radiation, as it is the leading indirect effect that damages DNA. Also, the use of Auger electrons, which

produces a cascade of events, will be more likely to produce a free radical species at some point.

In this project, only the Auger electrons from the radionuclides are being considered for energy deposition; the photons are all negligible. This is because the range of these photons is greater than a few hundred nm, and will travel outside the region of interest. This is a realistic assumption as we are solely looking on the nanoscale of the energy deposition and damage. The photons all have large enough energies to where they would not affect the cell that the nanoparticle attaches to, so they are not being considered. We are only interested in the Auger electron cascades and how they affect the cell.

Geometrical models of DNA can be used to view how the particles will interact with various DNA molecules, and other molecules within the cell, generally modeled as water. This work with Geant4-DNA is very important to radiobiology and future cancer therapy treatments, as it deals with the potential use of Auger electrons in cancer treatment.

3. RESULTS

One of the most important features about Geant4-DNA is that radioactive decay is modeled as independent, single events. Particulate emissions are not average estimates, and the energy of each emitted particulate is estimated based on ENSDF library using Monte Carlo methods (*135, 136*). Figure 12 and 13 show a comparison on the electron emissions calculated by Geant4 with those found in the open literature.

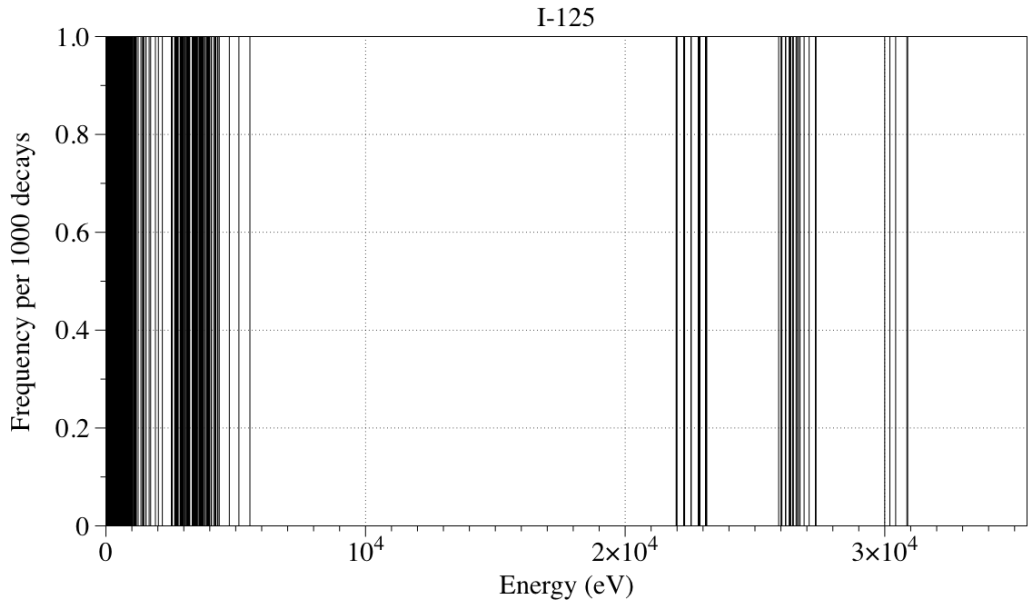

Figure 12. Energy of electrons emitted by ^{125}I for 1000 independent decays. The calculations were based using Geant4-DNA Radioactive Decay routine (*136*).

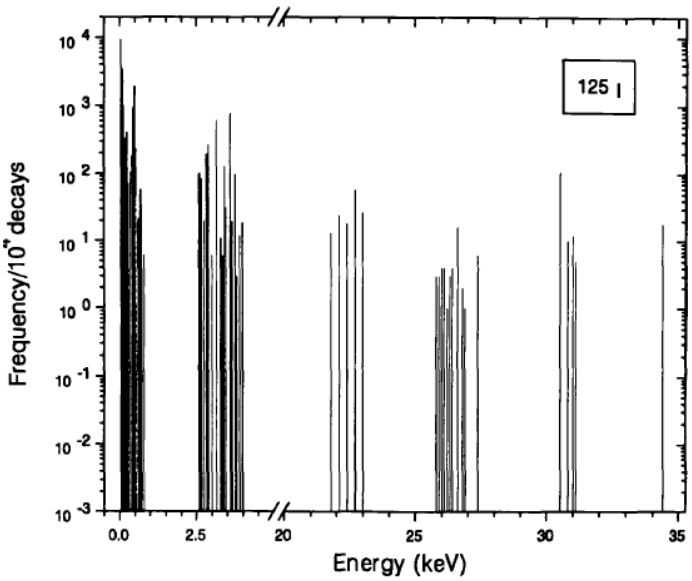

Figure 13. Average energies of electrons emitted by ^{125}I for 10^4 decays. These energies were calculated using theoretical methods (*137*).

Figure 12 shows the electron energies from the decay of ^{125}I simulated in Geant4-DNA, and Figure 13 shows electron energies from the decay of ^{125}I from previous calculations (*137*). The same clusters of electron energies are present in both graphs, proving that Geant4-DNA consistently simulates the decay of ^{125}I. Geant4-DNA code tracks each decay to completion, and the decays are independent. With this, the energy deposition from the radioactive atoms within the nanoparticles can be assessed. The y-axis is not normalized in Figure 12; it simply goes to 1 because each energy peak shown is sampled independently. The energies are not averaged together, like Figure 13, so each bar shown in a separate decay. One thousand decays were simulated due to computational time. Running the code with 10^4 decays was not plausible at the time.

Geant4-DNA was used to simulate the decay of ^{117m}Sn, as well. Figure 14 shows the frequency of the electron energies from the simulation of 1000 decays, as it was computationally efficient. Again, the y-axis is not normalized; it shows the frequency of a specific energy occurring from radioactive decay. Since these electron energies are not averaged, and are independently selected from the ENDSF library, the figure shows the discrete electron energies emitted from the decay of ^{117m}Sn.

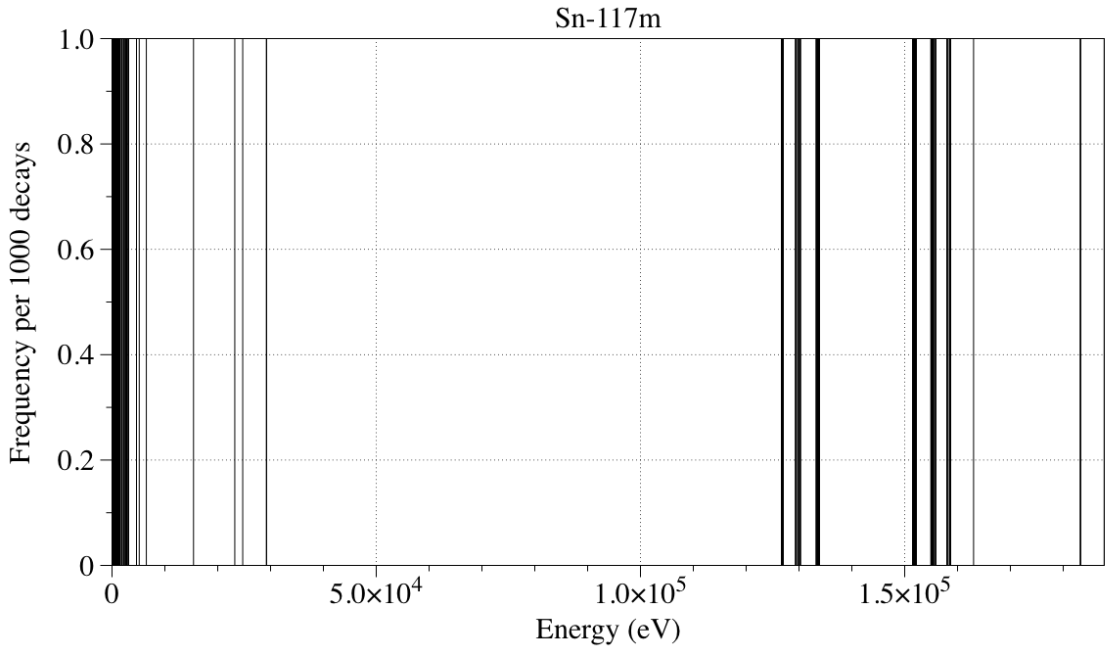

Figure 14. Energy of electrons emitted by ^{117m}Sn for 1000 independent decays. The calculations were based using Geant4-DNA Radioactive Decay routine (*136*).

Figure 15 shows the comparison of the electron energies emitted via radioactive decay of the two radionuclides.

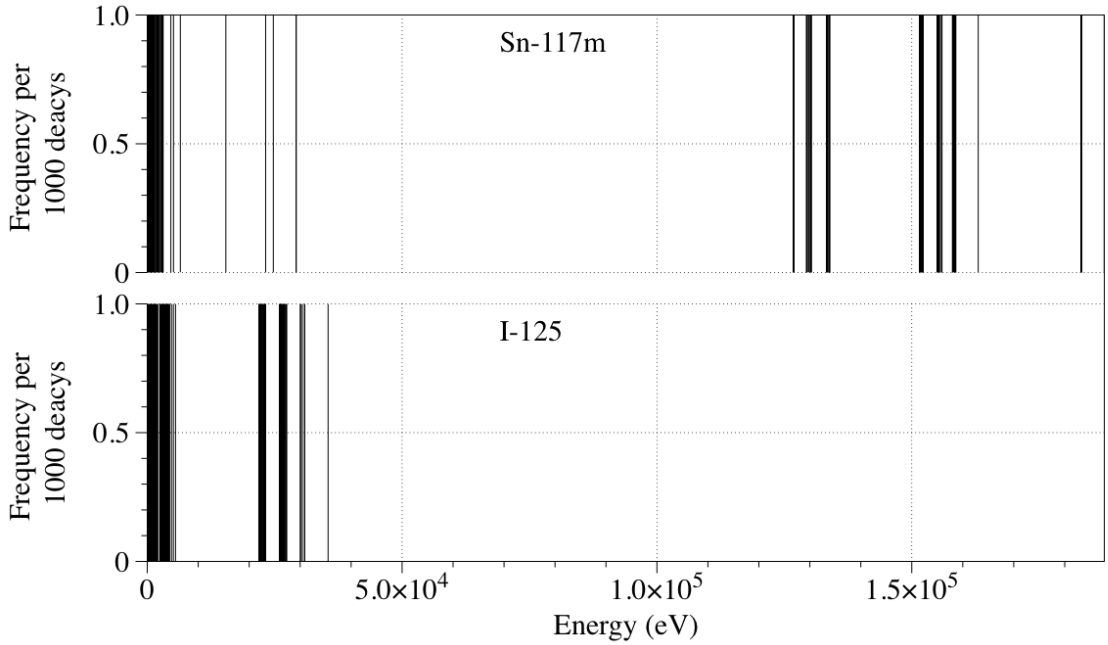

Figure 15. Energy of electrons emitted by ^{125}I and ^{117m}Sn. 1000 decays were simulated using calculations based on the Geant4-DNA Radioactive Decay routine (*136*).

Graphs were also created to easily visualize the energy of the electrons, and the frequency they occur at. Figures 16-19 below show the data from this perspective, with ^{125}I and ^{117m}Sn combined on the same plot. Each successive plot shows a different energy range. In Figure 16, the energy thresholds for the ionization of both gold and water are shown, for reference.

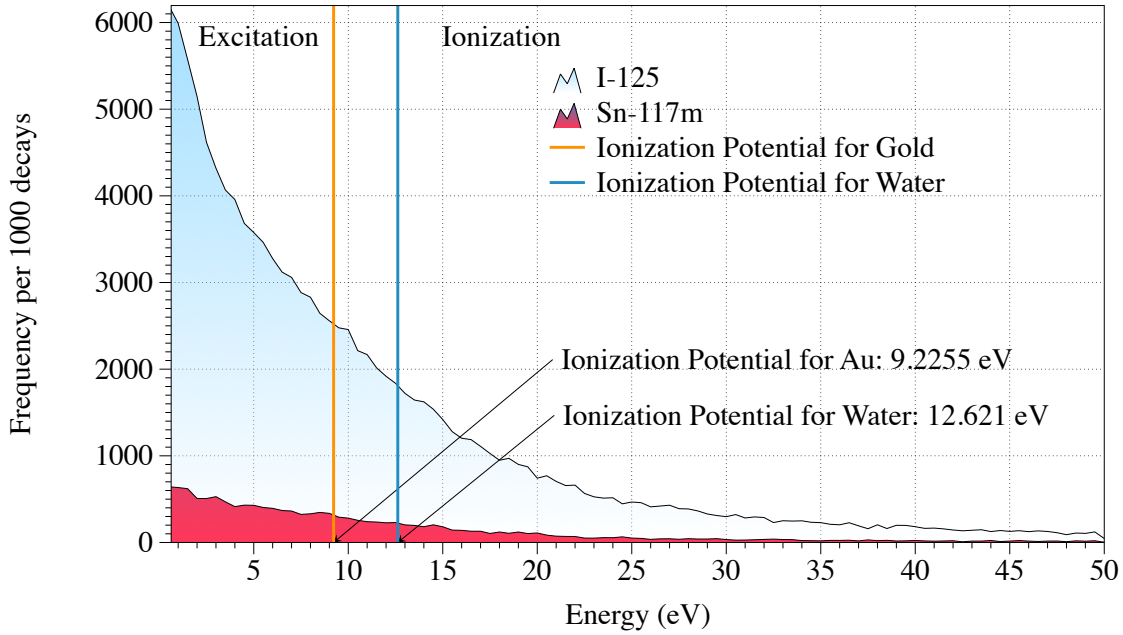

Figure 16. Electron energy plot for ^{125}I and ^{117m}Sn in 0-50 eV energy range.

Figure 16 shows the energies of the electrons emitted from the radioactive decay of the radionuclides studied. The blue curve represents ^{125}I and the pink curve represents ^{117m}Sn. The detailed energy range viewed is from 0-50 eV. It can be seen that a large portion of the electrons from ^{125}I are under the threshold for ionization of gold, so they will go on to liberate free radicals from the gold. This process is described later.

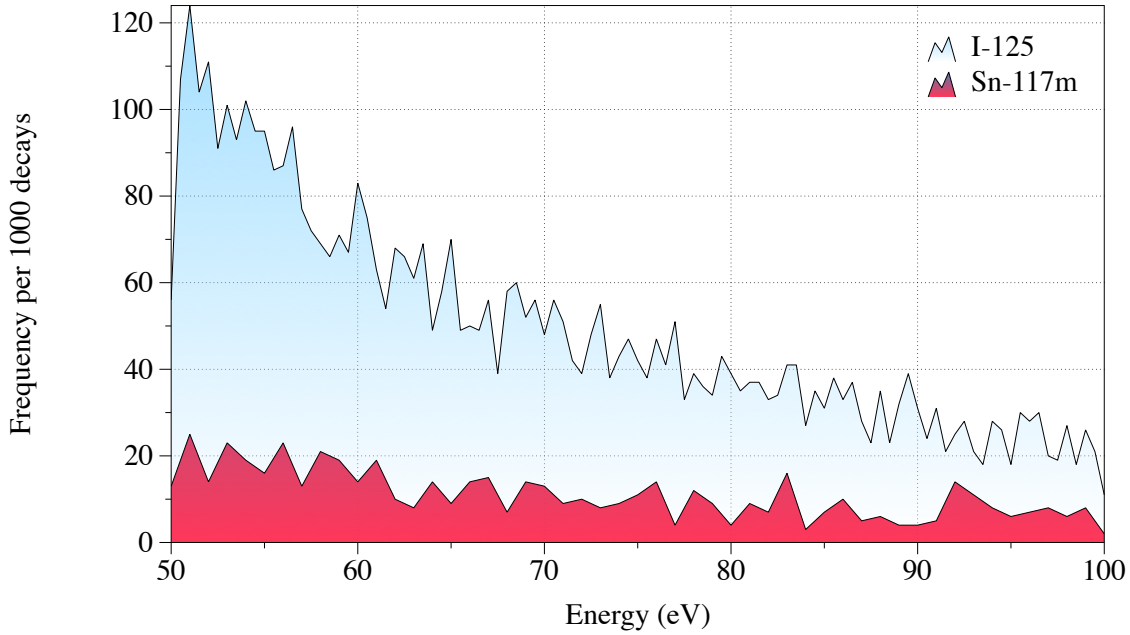

Figure 17. Electron energy plot for ^{125}I and ^{117m}Sn in 50-100 eV energy range.

In Figure 17, the specific energy range of 50-100 eV is shown. This graph shows that a larger number of electrons are emitted from ^{125}I compared to ^{117m}Sn in this energy range.

Figure 18 is the next continuation to the previous two figures, showing the electron energies in the range of 100-1000 eV. Again, it can be seen that there are more electrons emitted from ^{125}I in this energy range. For both radionuclides, after 600 eV there are few electrons emitted.

The last energy range shown is 1000-10000 eV, graphed in Figure 19. There are peaks of electrons emitted around 3000 eV for ^{125}I, and electrons emitted around 2000 eV for ^{117m}Sn, which steadily decrease.

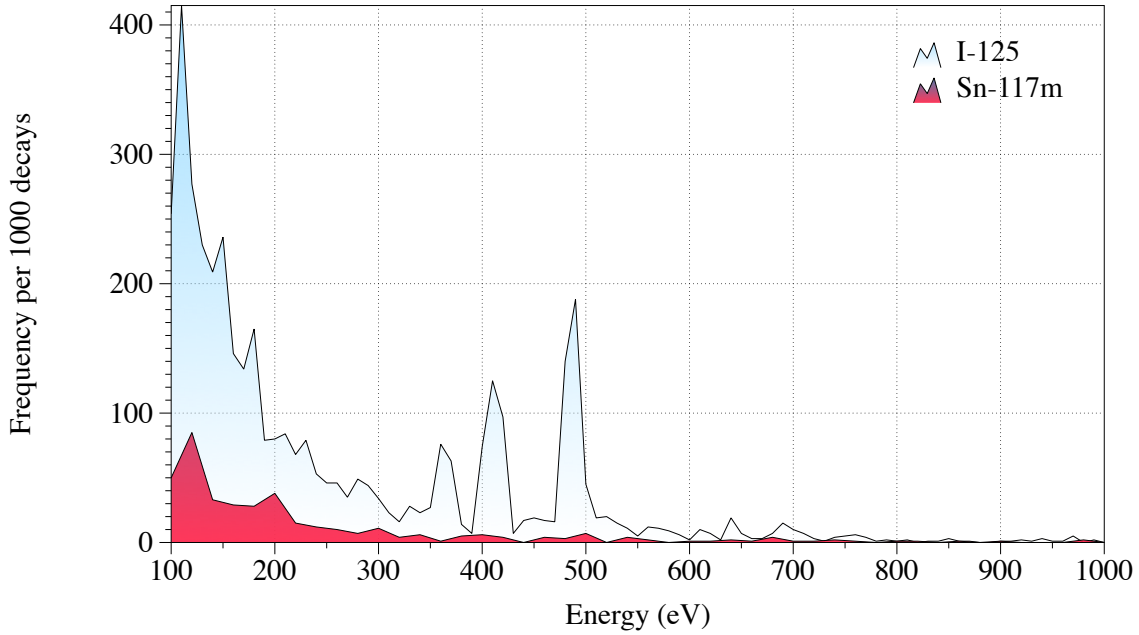

Figure 18. Electron energy plot for ^{125}I and ^{117m}Sn in 100-10^3 eV energy range.

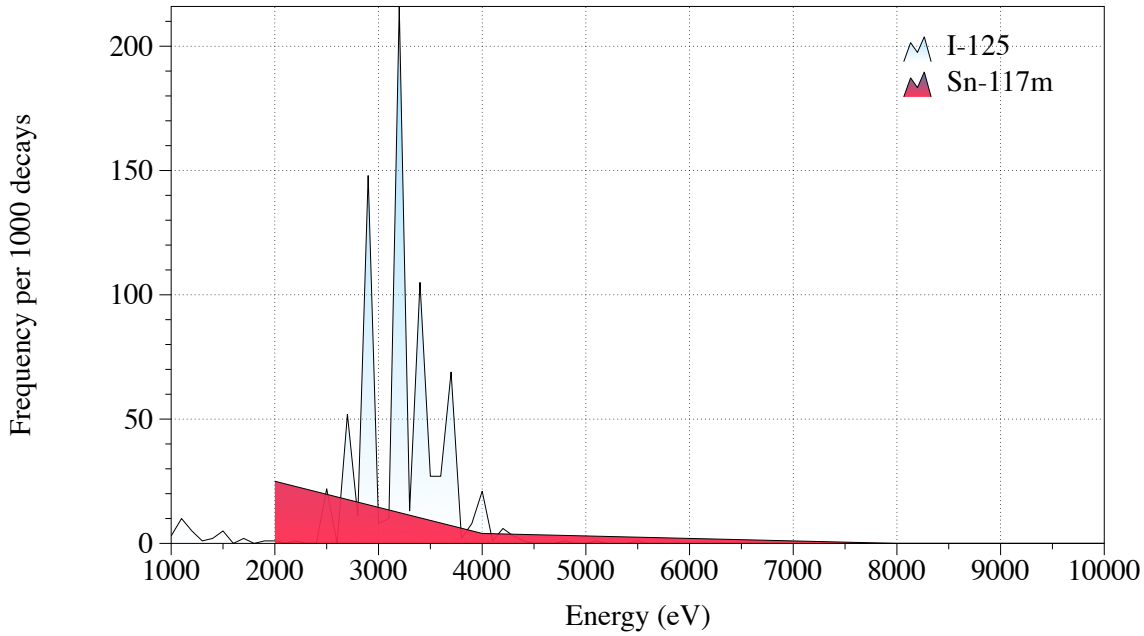

Figure 19. Electron energy plot for ^{125}I and ^{117m}Sn in 10^3-10^4 eV energy range.

As described above, Geant4-DNA was employed to simulate the decay of both ^{125}I and ^{117m}Sn radionuclides within a gold nanoparticle. The radioactive atom was placed in the center of the gold nanoparticle, so the energy deposition could be viewed surrounding each nanoparticle. From this, it could also be seen how far the electrons would need to travel, at the greatest case. The radius of the nanoparticle was modeled to be 15 nm. This radius was chosen to make the nanoparticle small enough for physiological reasons. Each simulation contains a single decay, and follows it through the whole track taking into consideration secondary particles produced. From these simulations, files were made to use in VisIt. The images below from VisIt show the energy deposition for various simulations.

In the images below from VisIt, the volume functionality was used to visualize the energy deposition values and locations from the decay of the radionuclides. The splatting method was chosen for rendering purposes, and within that 90,000,000 samples were used. This divides the data into smaller bins, so a more accurate assessment of energy deposition can be seen. With less samples, the data is averaged together, so using a higher number of samples will help to visualize the data more accurately.

The energy depositions shown in Figures 20-33 are in units of eV. These energy depositions were recorded in a specific location, such that the x, y, and z positions were attributed to a specific energy deposition.

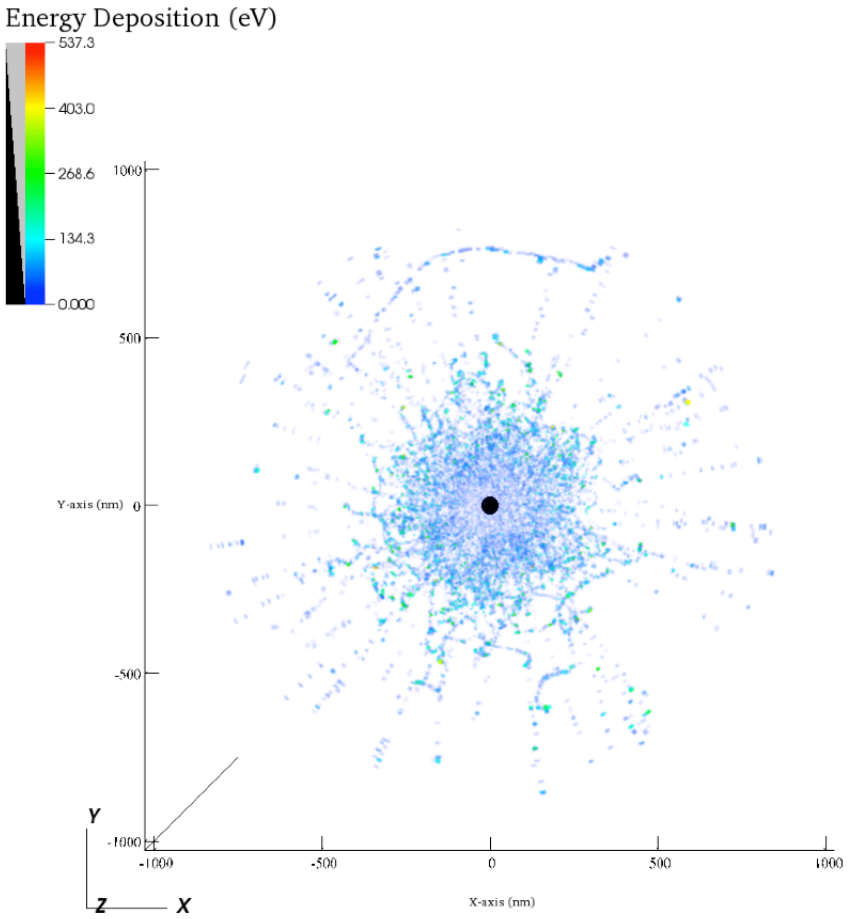

Figure 20. Energy deposition from 1000 independent decays of ^{125}I. The nanoparticle mesh is shown in the center of the image. 90,000,000 samples were used to create this image.

In Figure 20, the energy deposition is very dense in an immediate 250 nm radius around the nanoparticle. There are spots of green that form a ring around the energy deposition, where the Auger electron deposits the bulk of its energy. There are also smaller energy depositions that occur along the Auger electron tracks. The individual decays simulated in Geant4-DNA also had files associated with them to be used in VisIt, for visualization and analysis purposes. There are visible lines near the top of the image,

which could be an artifact of the number of VisIt samples used, or the random number generator in Geant4-DNA.

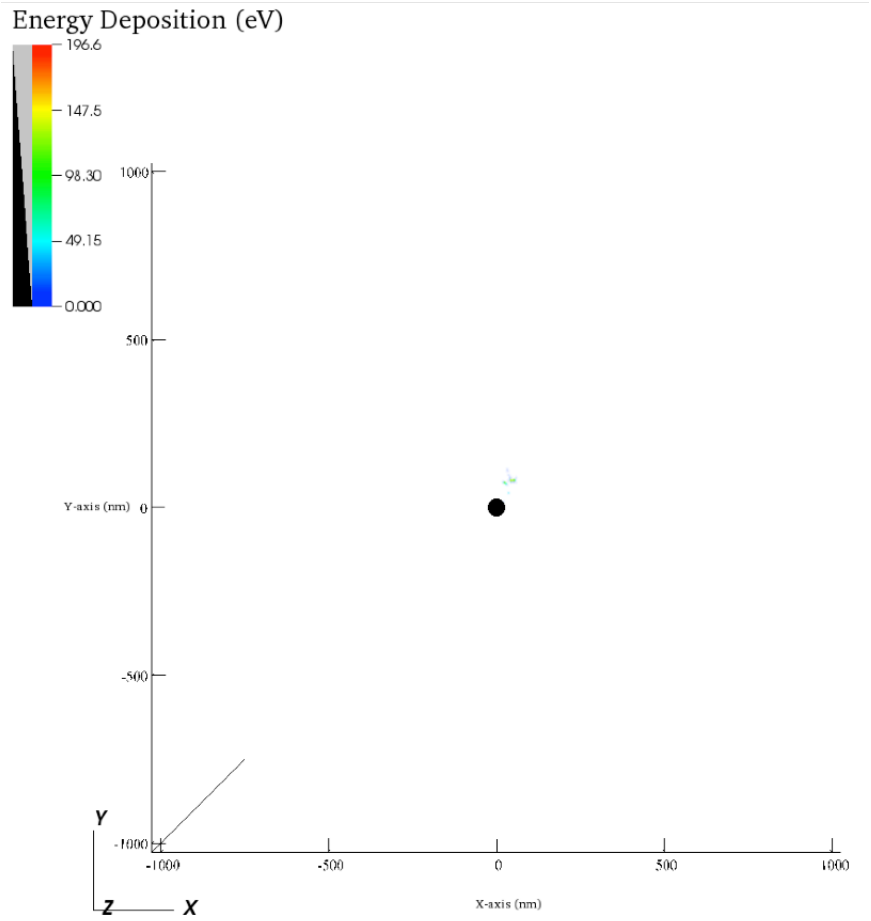

Figure 21. Energy deposition from a single decay of ^{125}I. The nanoparticle mesh is shown in the center of the image. 90,000,000 samples were used to create this image.

From Figure 21, it can be seen that the energy deposition from one decay of ^{125}I is quite strong. The energy deposition is quite clustered, occurring in about 100 nm. The energy deposition goes as high as 100 eV, which has important effects for therapy. This

energy deposition could potentially be targeted specifically towards the DNA, which would cause a large amount of damage.

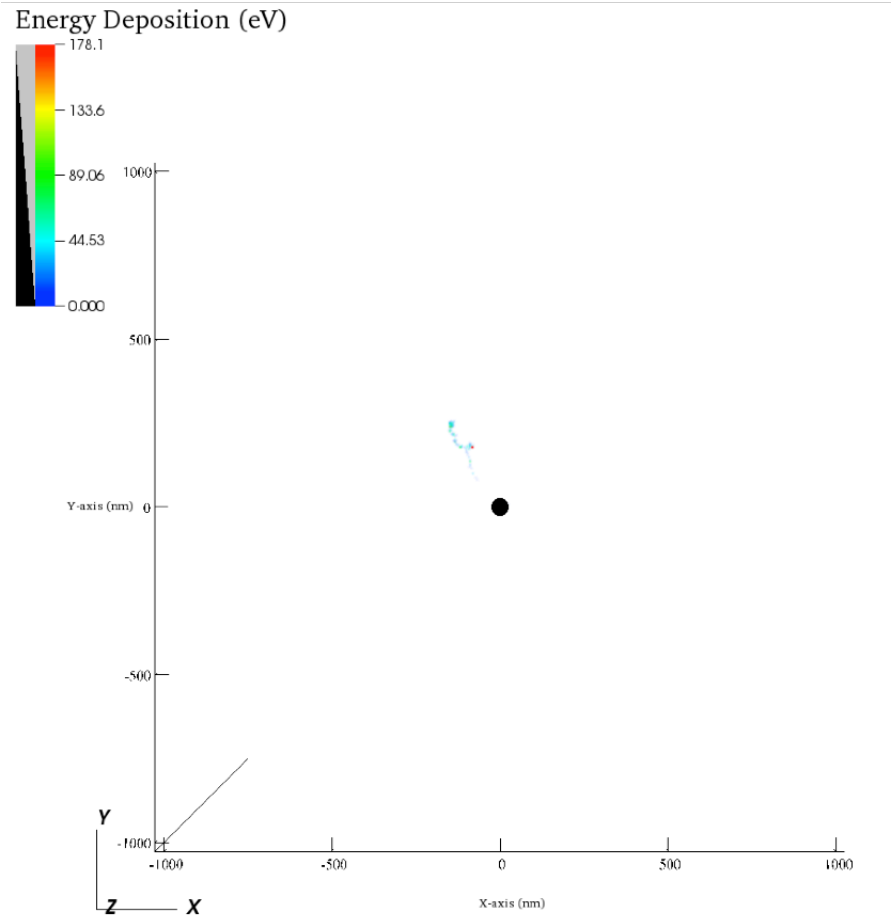

Figure 22. Energy deposition from another single decay of ^{125}I. The nanoparticle mesh is shown in the center of the image. 90,000,000 samples were used to create this image.

In Figure 22 a different ^{125}I atom decay is shown. There are more sites of deposited energy, compared to Figure 21, and there is a spot where about 178 eV of energy deposition. Apart from this large bulk deposition, there are smaller energy

depositions along the track, about 40 eV, followed by a bulk deposition around 90 eV at the end of the track, typical of Auger electrons.

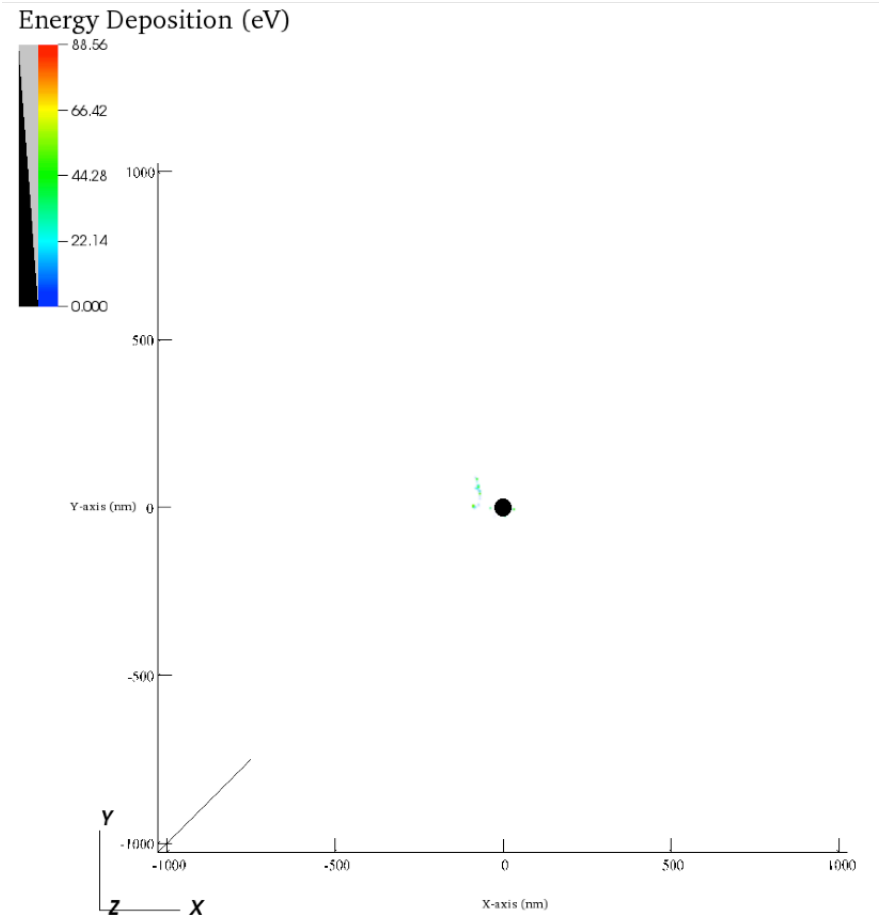

Figure 23. Energy deposition from a third single decay of ^{125}I. The nanoparticle mesh is shown in the center of the image. 90,000,000 samples were used to create this image.

The energy deposition shown in Figure 23 is much more clustered than either Figure 21 or Figure 22, with some particles escaping the gold nanoparticle to release energy right next to it. The average energy liberated at these sites is about 44 eV.

The next set of plots that are important to consider for the therapeutic use of gold nanoparticles containing radioactive atoms is the energy contour plots.

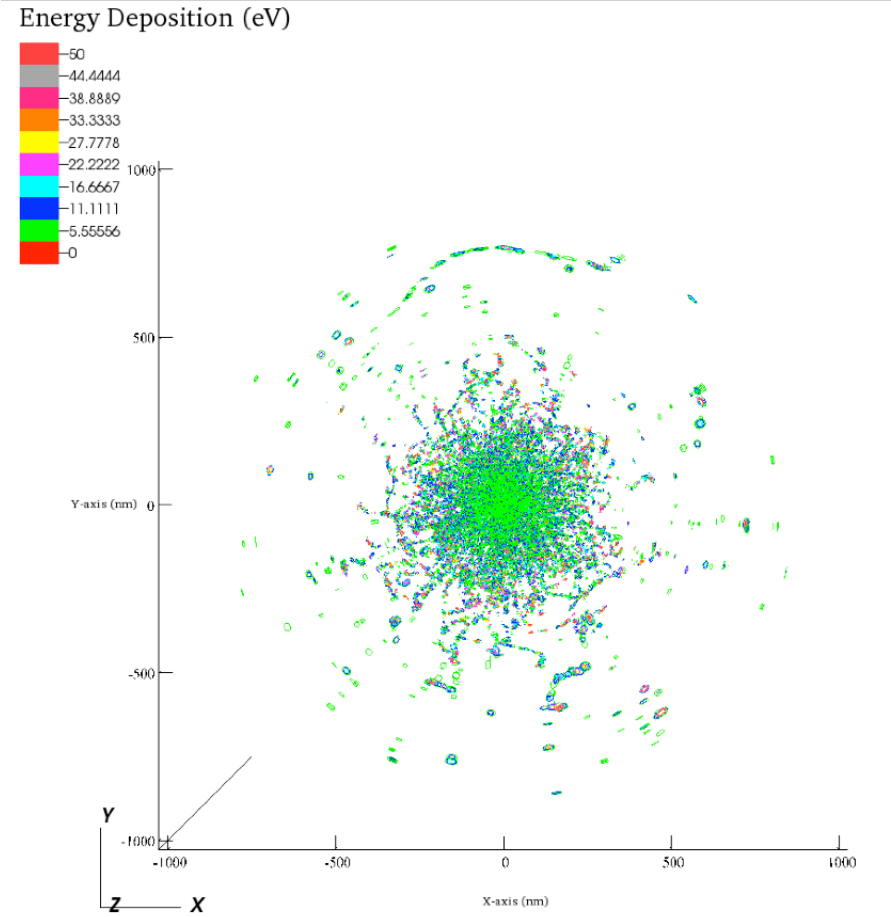

Figure 24. Energy contour for 0-50 eV of ^{125}I. 90,000,000 samples were used to create this image.

Figure 24 shows the contour for ^{125}I from the energy deposition values from Figure 20, with only energies in the of 0-50 eV. Energies higher than 50 eV were removed from this specific contour, to obtain the locations of the lower energy

discharges. A significant amount of damage will come from these low energy electrons, so it is imperative to know the location of where they will be. The cluster of low energy deposition can again be seen in a radius of 250 nm. At the edge of this cluster, the higher energy depositions can be seen even more clearly.

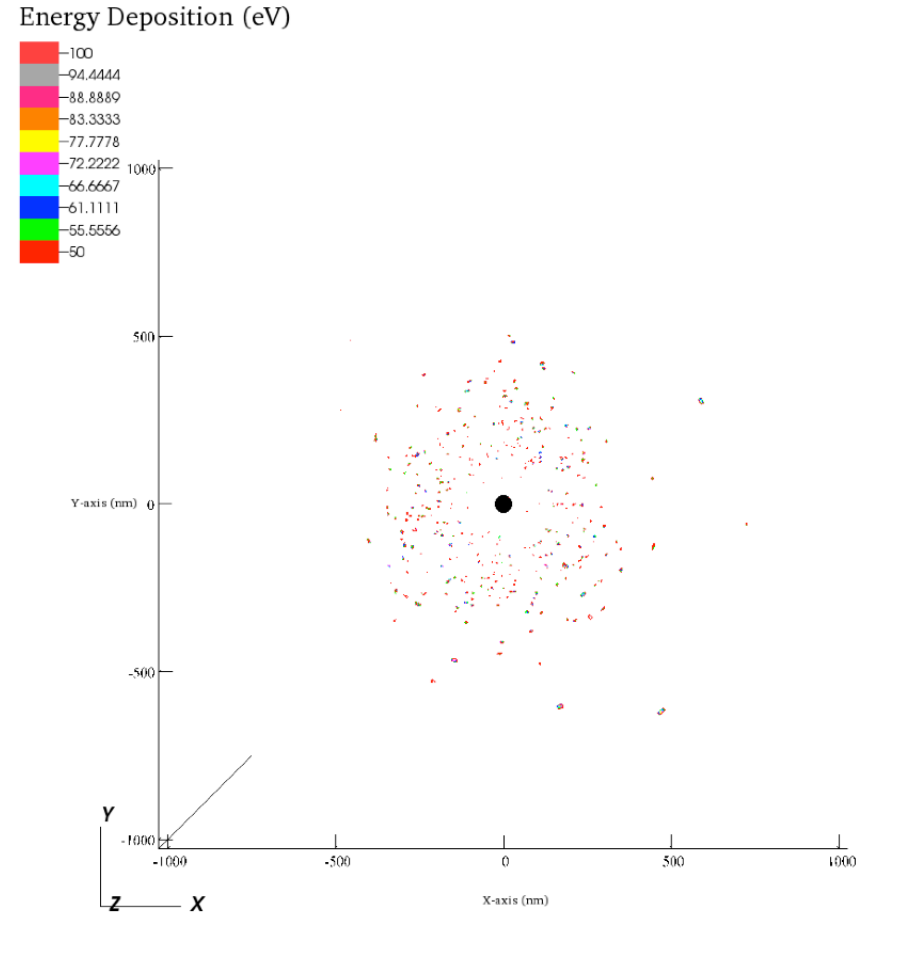

Figure 25. Energy contour for 50-100 eV of ^{125}I. 90,000,000 samples were used to create this image.

Figure 25 shows the contour of energy deposition for the ^{125}I decays in the 50-100 eV range. Any energy depositions that were less than 50 eV and greater than 100 eV were hidden. It can be seen that most of this energy deposition occurs within a ring, from about 100-500 nm. There are several sparse energy depositions beyond 500 nm, but the majority of energy is depositing within the ring.

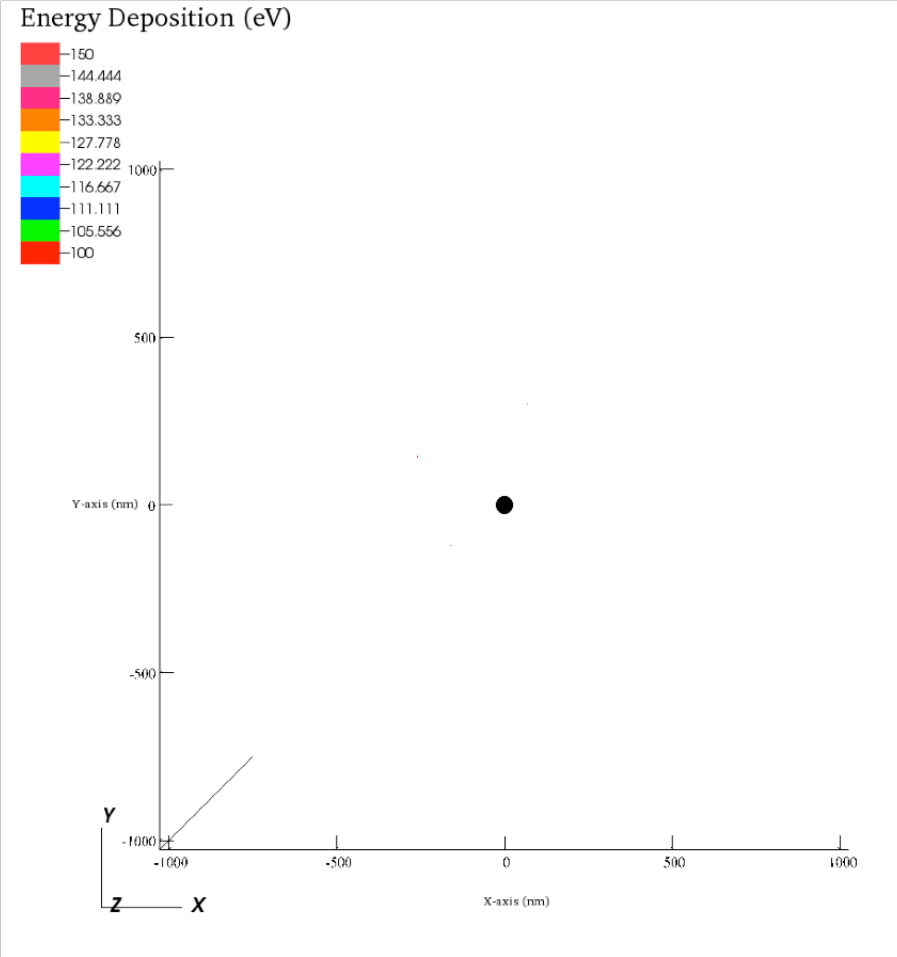

Figure 26. Energy contour for 100-150 eV of ^{125}I. 90,000,000 samples were used to create this image.

In Figure 26, the contoured energy deposition for the energy level of 100-150 eV can be seen. These occurrences are very sparse. Most of the energy from the Auger electrons is lower, and has already been released.

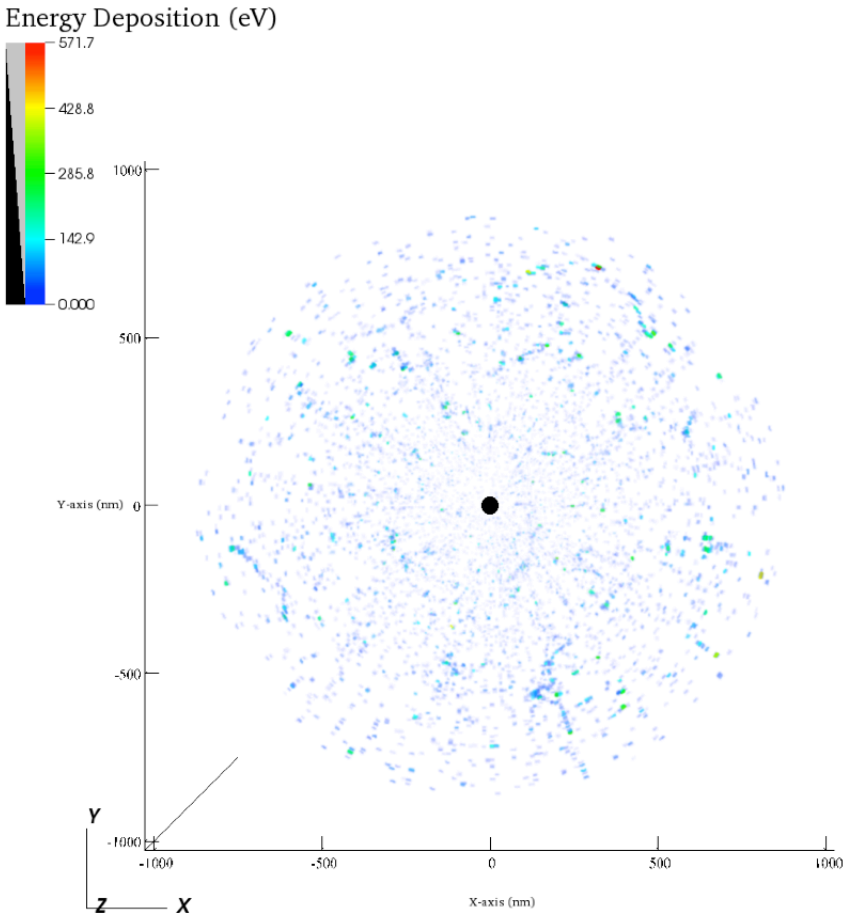

Figure 27. Energy deposition from 1000 independent decays of ^{117m}Sn. The nanoparticle mesh is shown in the center of the image. 90,000,000 samples were used to create this image.

Figure 27 shows that the energy deposition from this radionuclide is much more sparse, compared to the energy deposition from ^{125}I. Based on the energy deposition histograms, this is to be expected. There were more low energy electrons present in the decay of ^{125}I, which are visibly clustered near the nanoparticle. In this decay, there are groups of higher energy electrons, although fewer, which is why the energy deposition is sparser, but located further from the nanoparticle. There are denser regions of energy discharge however where an electron tracks have been produced. These tracks generally end with a green dot, which indicates a larger energy deposition around 285 eV. This is characteristic of Auger electrons. The following figures show several individual decays of ^{117m}Sn atoms, as it is important to understand how much energy will be released from these decays, and where it will occur.

The particular decay shown in Figure 28 is interesting, due to the long range of the electron emitted in the radioactive decay. About 78 eV is deposited in several locations along the electron track, followed by a bulk deposition up to 157 eV. This is a typical Auger emission, defined by its short track length and bulk amount of energy deposited at the end of the track.

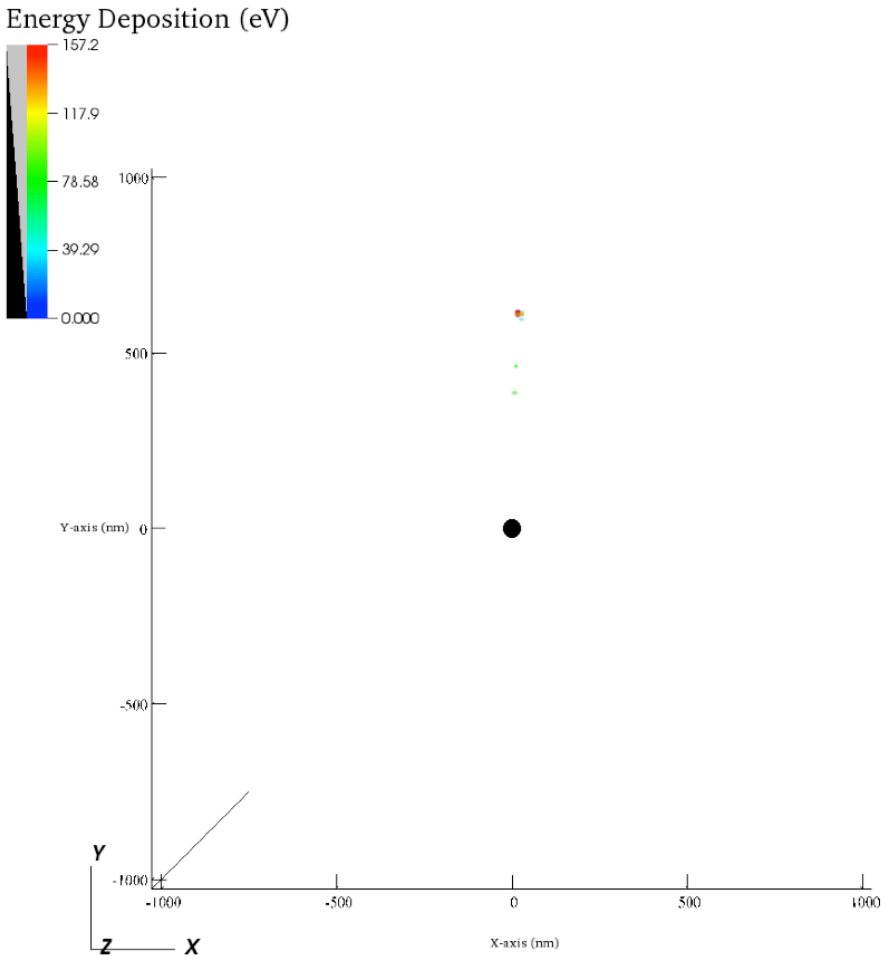

Figure 28. Energy deposition from a single decay of ^{117m}Sn. The nanoparticle mesh is shown in the center of the image. 90,000,000 samples were used to create this image.

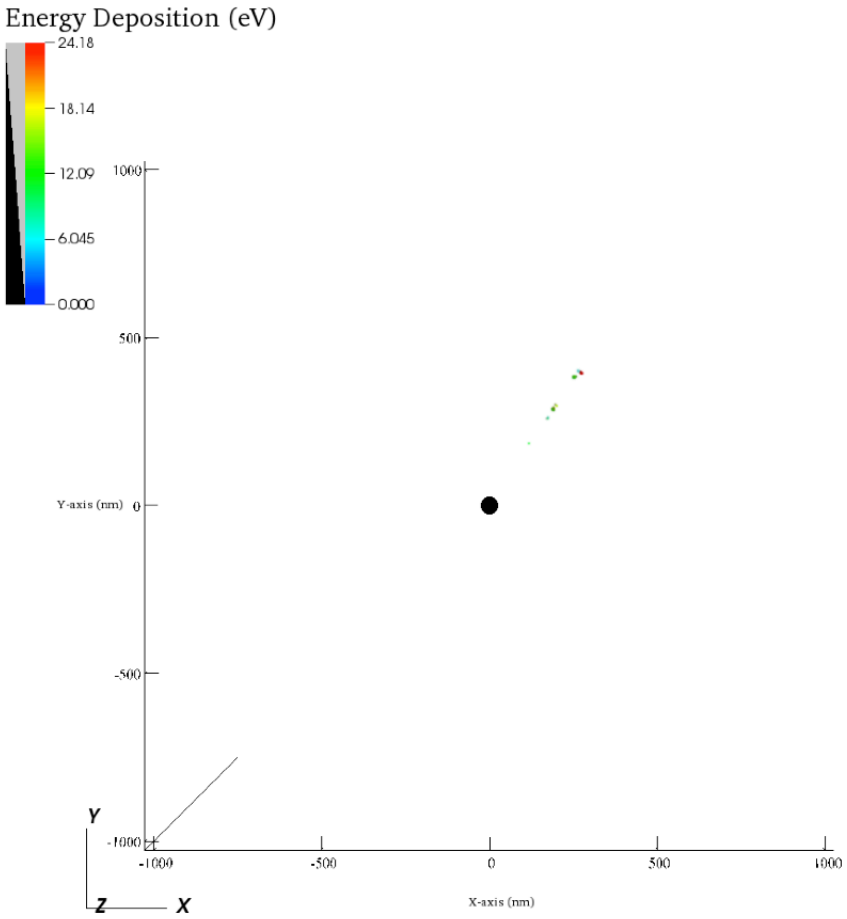

Figure 29. Energy deposition from another single decay of ^{117m}Sn. The nanoparticle mesh is shown in the center of the image. 90,000,000 samples were used to create this image.

In Figure 29, an energy deposition very similar to that of Figure 28 can be seen, although overall with lower energies. There are a few more spots of energy deposition along the track, with the typical majority of the energy deposited at the end.

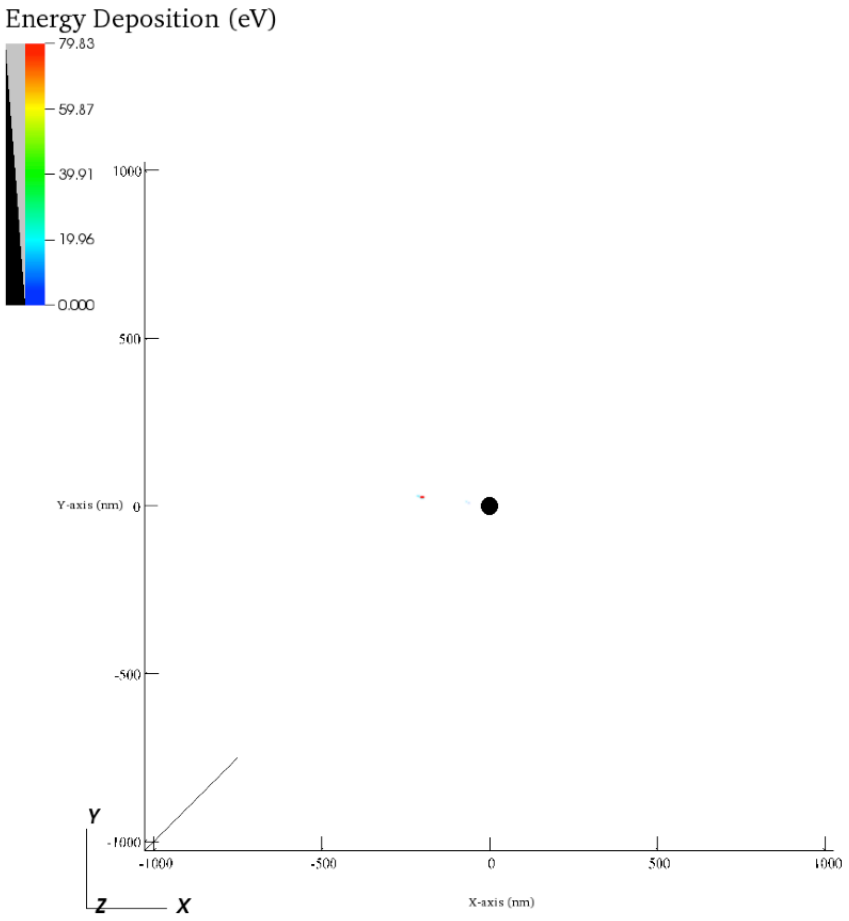

Figure 30. Energy deposition from a third single decay of ^{117m}Sn. The nanoparticle mesh is shown in the center of the image. 90,000,000 samples were used to create this image.

Figure 30 shows the energy deposition for another independent decay of ^{117m}Sn. This is more sparse than both decays shown in Figure 28 and Figure 29, with only two locations of energy deposition around 40 eV, and a third location, where double that amount of energy was deposited.

The energy deposition contours were then plotted to visualize the locations and probabilities in different ranges of energies. These contours were broken up into three groups, and can be seen below in Figures 31-33.

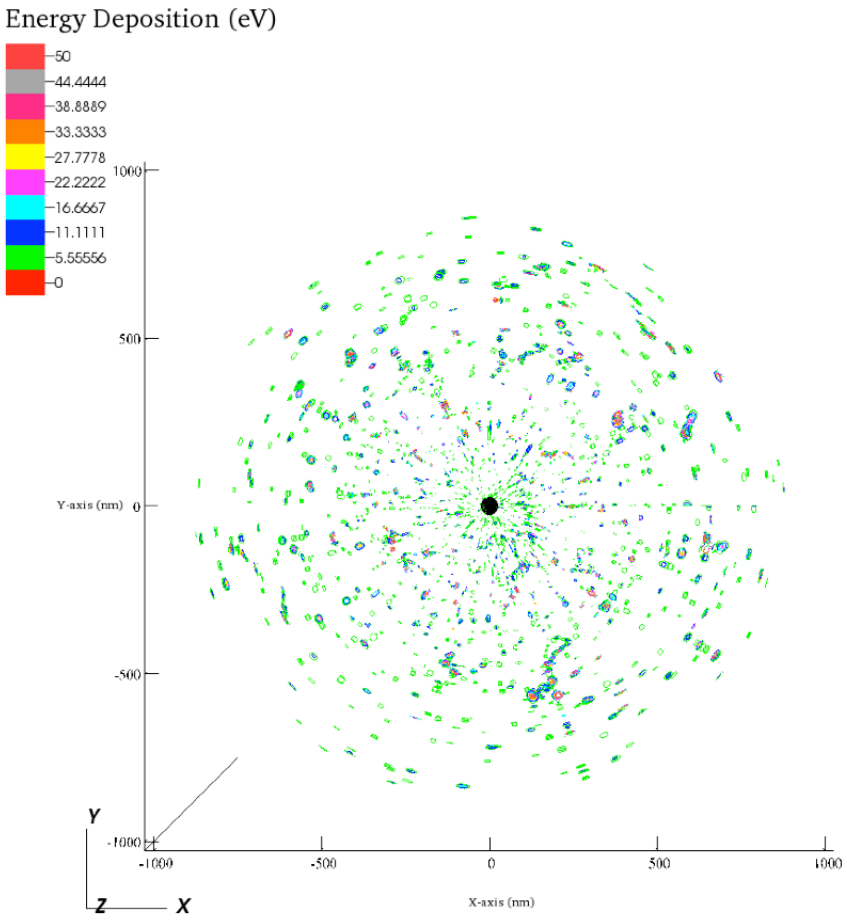

Figure 31. Energy contour for 0-50 eV of ^{117m}Sn. 90,000,000 samples were used to create this image.

Figure 31 shows the contour for the energy deposition from the decay of ^{117}Sn atoms in the energy range of 0-50 eV. In this contour, any energy that was greater than

50 eV was removed, for the purpose of obtaining the locations of the lower energy releases. From the contours, it is easy to see the characteristic Auger electron tracks. The majority of the track is green, symbolizing a smaller energy deposition, followed by a large bulk deposition at the end of the track, going up to 40 or 50 eV in some cases.

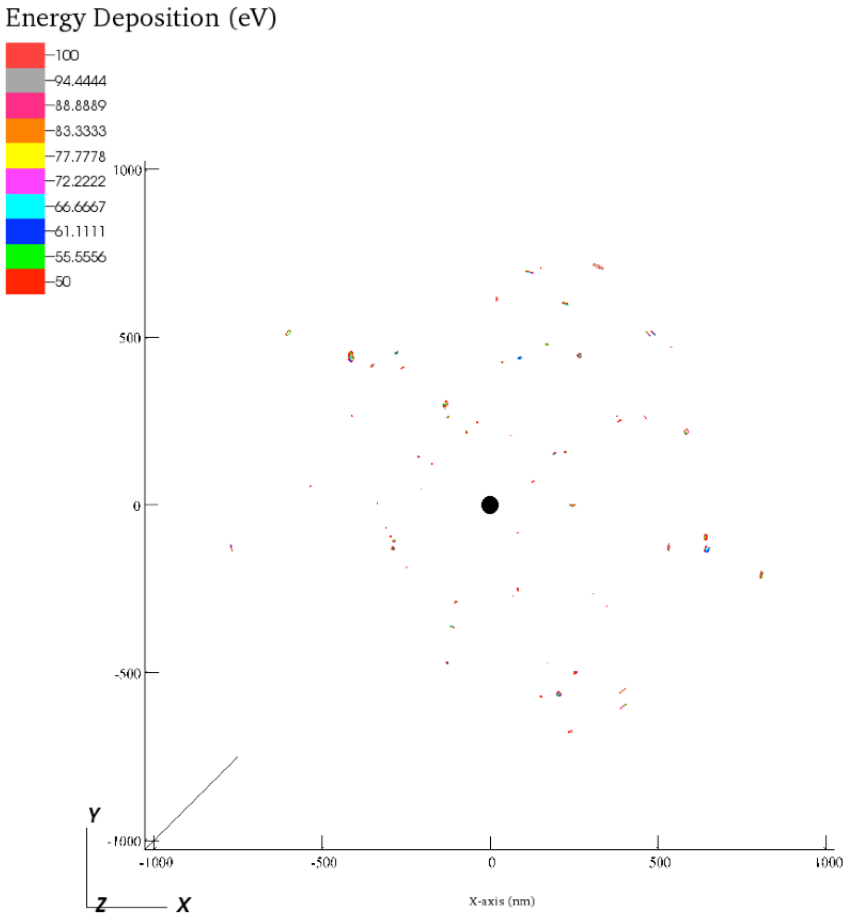

Figure 32. Energy contour for 50-100 eV of ^{117m}Sn. 90,000,000 samples were used to create this image.

In Figure 32, the contour is shown for energies in the range of 50-100 eV and energies not within this range were excluded from this plot. These are the middle energies, and it can be seen that they are further away from the gold nanoparticle. This is because these electrons have a longer range, due to their higher energies, and are able to travel further. Compared to the other radionuclide, ^{125}I, the energy depositions are much more sparse. This is to be expected, based on the decay schemes.

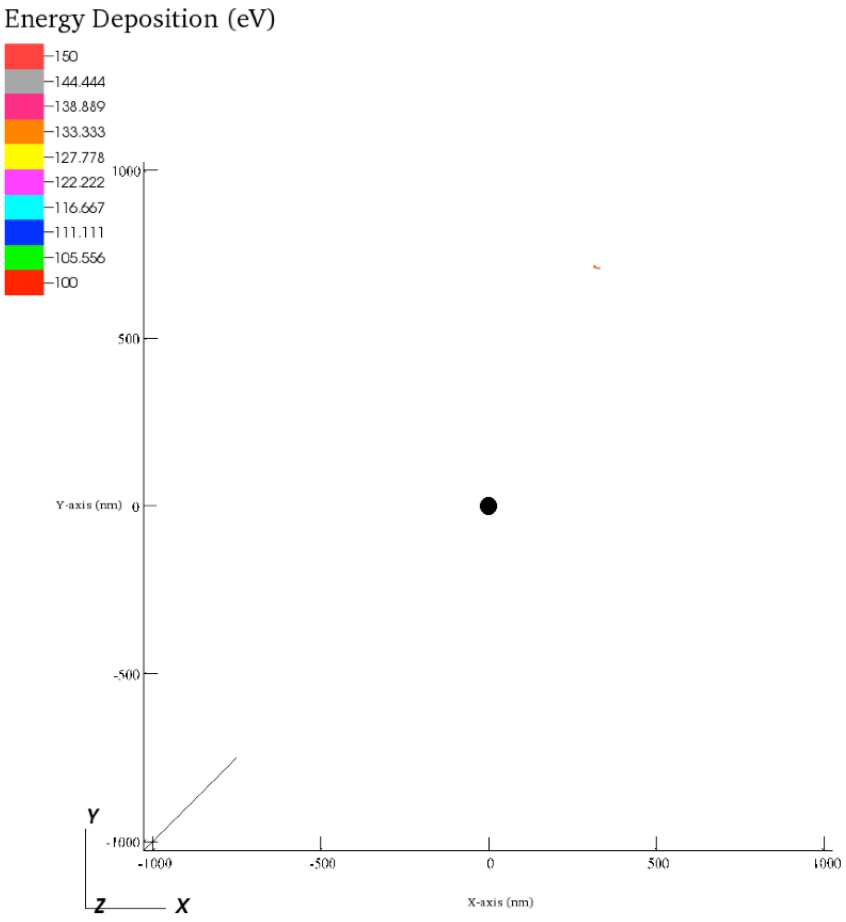

Figure 33. Energy contour for 100-150 eV of ^{117m}Sn. 90,000,000 samples were used to create this image.

From these simulations, there was only one spot of energy deposition within the range, however, it was significantly larger than the spots found in the contour for the same energy range of the other radionuclide studied. In Figure 33, the energy deposition at this location is around 130 eV, if not larger, with approximately a 100 eV deposition in the center.

It is important to note that in Figures 20-33 above, while the electrons look like they escape the nanoparticle, this may not be the case. In Geant4-DNA, the only available medium is water, so the nanoparticle was modeled as water. However, the nanoparticle is actually composed of gold and will attenuate most of the lower energy electrons, so they will not escape, and thus not be seen in visualizations of the data. In the discussion below, these changes are accounted for.

4. DISCUSSION

4.1 Predicate Studies with Gold Nanoparticles as Dose Enhancers

There have been numerous studies where gold nanoparticles have been used as dose enhancers or radio-sensitizers where low energy electrons are produced by the interaction of orthovoltage or megavoltage x-ray or high energy electrons with gold nanoparticles, gadolinium, and rare earth metals where in vitro experimental studies have shown that gold nanoparticles are capable of producing an enhanced cytotoxic effect (*138-149*). In these studies the nanoparticles are used as radiation dose modifiers or enhancers by producing photoelectron, Auger electrons, and fluorescent x-rays that further interact with tissue.

On the other hand, the present research is focused in studying the effects of radioactive decay of Auger electron emitting radionuclides ^{125}I and ^{117m}Sn within a gold nanoparticle and assessing the dosimetry effects. Whereas the use of x-rays is limited to a well-defined anatomical structure within the radiation field in solid tumors, the use of functionalized radioactive nanoparticles allows for the treatment of minimal residual disease, MM and CTC as a targeted radionuclide therapy.

4.2 Electron Ranges & Electron-Hole Recombination

From the histogram showing the electron energy distribution, it can be seen that a large portion of the electrons will have a very low energy, under 10 eV. With this, it is important to calculate how much energy will actually escape the nanoparticle to be deposited within the MM. For this model, it is assumed that the gold has a density of 20

g/cm^3, and water a density of $1g/cm^3$. The nanoparticles modeled in this simulation have a radius of 15 nm, but they can be manufactured with different diameters. Various radii are used for gold nanoparticles, as seen in the table below. The radioactive atom is placed within the nanoparticle, and the electrons emitted from the decay must travel within the gold first, to escape outside into the water. Table 9 shows the radius of the gold nanoparticle, and the corresponding distance the electron would have to travel in water. The assumption was made that multiplying the radius of the gold by the density of gold would give a reasonable estimate for the same distance in liquid water. Due to the electron density differences between these two materials however, this is a rough estimate. Figure 36 portrays a more accurate relationship between the electron energy and range in gold.

Table 9. Electron range as a function of energy.

Gold (radius)	Water (radius)	Electron Energy
5 nm	100 nm	250 eV
10 nm	200 nm	550 eV
15 nm	300 nm	2000 eV

This information is important to have and understand. The corresponding electron energies must be known for these ranges. As shown above, the larger the radius of the nanoparticle, the higher the energy needed for escaping into the surrounding medium. Based on the electron energy histograms for the two radionuclides, there will be plenty of low energy electrons that do not escape, and go on to cause excitations and

produce free radicals from electron-hole pair recombination. However, there are also large portions of electrons that will have plenty of energy to escape, and will directly damage the DNA through the breaking of bonds, or indirectly damage the DNA through free radical production if the distance is too large. This phenomenon is important to consider because of the electron hole-pair recombination that occurs. This is when an electron and an electron hole (the pair, mentioned earlier) give up their combined energy to a third electron in the same conduction band, to recombine. When this occurs, the energy of the third electron is increased. This is known as Auger recombination. Figure 34 shows this phenomenon.

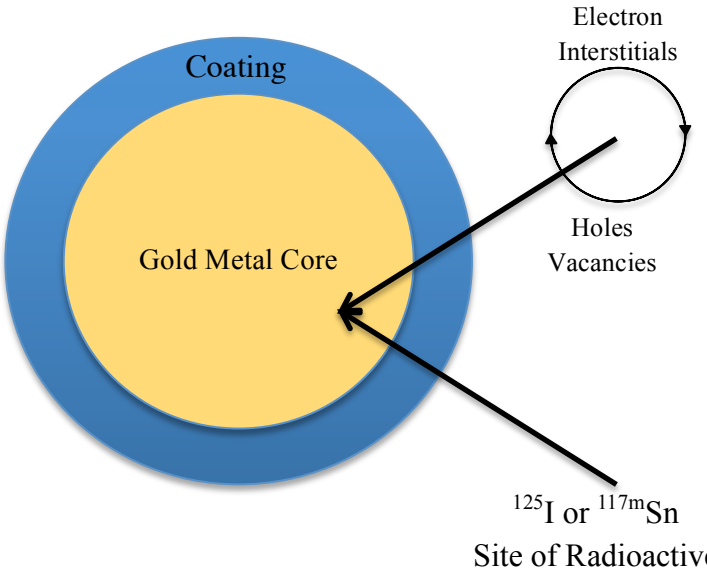

Figure 34. Gold nanoparticle schematic and recombination.

As previously stated, the third carrier is excited to a higher energy level, but does not move to a new band. The third electron generally gets rid of any excess energy though thermal vibrations. This can add heat to the nanoparticle, which must be taken into account. But with the amount of excitations occurring from recombination, and the higher energy electrons escaping, it is clear that this method is an effective therapeutic strategy.

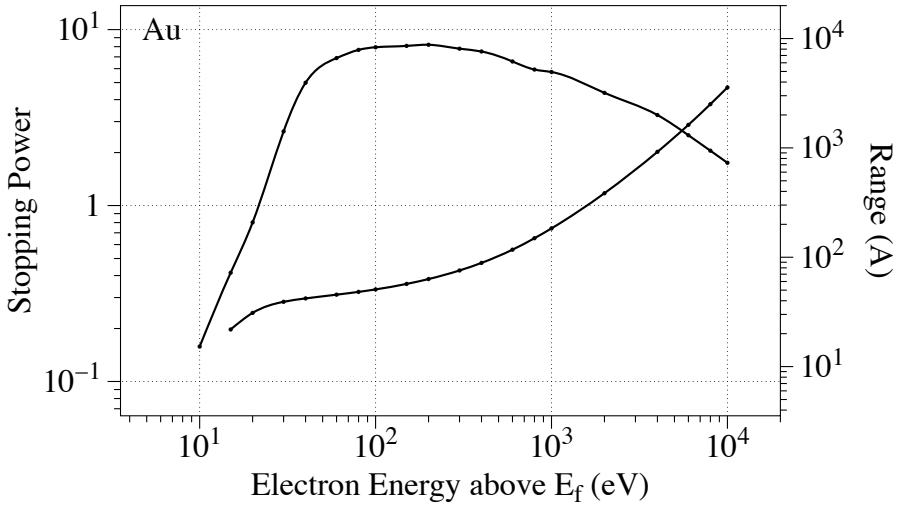

Figure 35. Stopping power and range as a function of energy.

The stopping power and range for the electrons is shown in Figure 35. The stopping power was integrated to find the range of the electrons in gold.

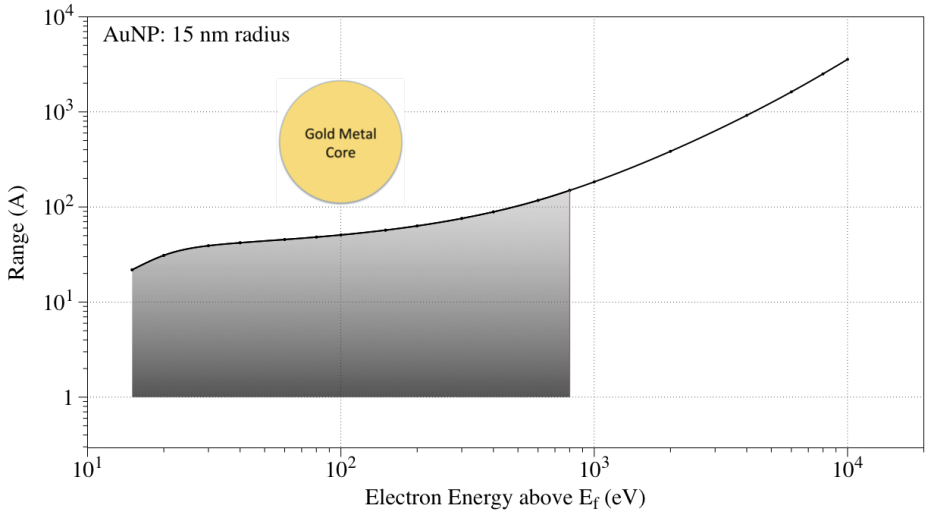

Figure 36. Range of electrons in gold as a function of energy.

Figure 36 shows the electron range in gold, as a function of electron energy. The nanoparticles modeled had a radius of 15 nm, which was found on the y-axis (range). Finding the corresponding energy, it can be seen that any electrons under 800 eV of energy will not escape the nanoparticle. These electrons will become part of electron-hole pair recombination, and become part of the radical generation that will take place at the surface of the gold nanoparticle.

From the information in Table 9 and Figure 36, after electrons with high enough energies escape the nanoparticle, the expected range would be on the order of a few hundred nm. Depending of the location of the nanoparticle, this would be plenty of energy to directly damage the DNA, or produce secondary particles in water radiolysis.

The number of excitations and ionizations generated inside the gold nanoparticle by the Auger electrons generate what is commonly referred as a Coulomb explosion

(*150*). This phenomenon has been suspected as the principal mechanism of direct damage of Auger emitting radionuclides. The gold nanoparticle will become highly charged, generating a significant Columbic potential that in turn will dissipate its energy to other molecules, including water. The charge buildup generated by the decay of ^{125}I and ^{123}I has been simulated by Kümmerle and Pomplun using models of 5-tellurouracil, 5-telluro-2'-deoxyuridine, and 5-telluro-2'-deoxyuridine-3',5'-biphosphate (*151*). Their results indicate that Coulomb explosion is a significant phenomenon that needs to be further experimentally studied.

4.3 Radiation Protection

There are very specific guidelines that must be followed when dealing with these radionuclides. The radiation protection that must be employed when using this radionuclide is straightforward and easy to follow. It is important to note that ^{125}I has a half-life of about 60 d, and emits a photon with a maximum energy of 0.035 MeV. ^{125}I is also known for its Auger electron cascade (*152*). The major concern when dealing with this radionuclide is unnecessary exposure. However, this can be handled in a few ways. The first step to protect against unnecessary exposure is to maintain the ALARA principle, and only work with the material when needed. Shielding should also be used, as this will drastically reduce the dose an employee or patient will get to an area that should not be exposed. Lead is used to attenuate photons, and can be used to reduce the amount of radiation to specific areas. Another precautionary step that can be taken is to wear lab coats and monitor dose with badges. ^{125}I can easily be detected with either a

sodium iodide scintillation detector or Geiger-Muller tube, so surveys should be done with either instrument to ensure that contamination has not occurred.

There are rules that should be followed when working with ^{125}I, so accidental exposures do not occur. There are also guidelines put into effect by the government, in 10 CFR 35, for dealing with ^{125}I, specifically applying to brachytherapy seeds (*153*). For example, the document specifies how the ^{125}I seeds should be handled. Since the use of nanoparticles would be handled in a similar manner, it is important to understand these procedures. They include having a trained and accredited radiologist handling the seeds, shielding the seeds pre-implantation, and making use of radiation warning signs. When dealing with any radioactive material, film badges should be used to supervise the dose the staff receives, as well as using appropriate protective garments and lead shields to reduce the dose.

In addition to the aforementioned techniques, certified personnel should perform swipe tests (*154*). Typically, a radiation safety officer will be at the facility to enforce NRC regulations and ICRP recommendations through treatment plans (*155*). Dosimetry of the specific situation along with calculated energy deposition should be calculated if further radiation protection is needed.

Although ^{117m}Sn has different physical characteristics including a 13.67 d half-life with an average photon emission of 158 keV, the protection should still be similar, as it too is an Auger emitter.

4.4 ^{125}I in Brachytherapy

When using radioactive iodine for therapy, it is not used alone, but rather in conjunction with other materials. In brachytherapy, ^{125}I is simply the source of energy. The seeds used in this procedure contain two main elements: the core and the shell. The core is coated in the radioactive isotope while the shell is a biocompatible material, usually titanium (*156*). The core is housed within the shell, which is then inserted into the tumor where it will remain. There are various materials and structures used in producing these seeds, and they vary by company. In other therapy types, such as treatment with radioactive nanoparticles, there are many compounds and solutions that go into the preparation of the nanoparticles. In this model, the gold nanoparticles are composed of a core of gold synthesized together with the radioactive iodine, to produce a uniform distribution of radioactive material inside the center. The gold nanoparticles are then coated with a substrate such as PEG, or polyethylene glycol, so they are not a biohazard when entering the body. The outer layer of the nanoparticles consists of different tagging agents to functionalize the nanoparticle, such as proteins or antibodies, to effectively target the correct position of the tumor so the nanoparticles can correctly attach (*157*).

This project is a type of brachytherapy, and can be considered brachytherapy on the nanoscale range. Brachytherapy is simply defined as a specialized type of radiotherapy, in which the radiation source is placed next to the treatment area. In this project, nanoparticles are used to treat the cancerous areas, and different types of solutions coat the nanoparticles to guide them to the areas where the tumors are located.

In doing this, the nanoparticles, containing radioactive material, deposits virtually all of their energy to the cancerous cells, in essence, brachytherapy on the nanoscale. The difference is that generally the energy in brachytherapy comes from photons, while in this model the energy deposition to the DNA will be done primarily through Auger electrons.

4.5 Energy Deposition

It is important to discuss the energy deposition from the gold nanoparticles in terms of how many electrons will escape the actual nanoparticle. In Geant4-DNA, the only medium available is water, so the whole system was modeled as liquid water. However, in reality, the electrons will have to travel through material that is almost 20 times denser than water, so not all the electrons will escape. Calculations were made above in Table 9, as to understand which energy electrons would be able to escape. It was found that the lower energy electrons would not escape nanoparticle, and will most likely give off thermal energy and excite other particles, through electron hole pair recombination. However, there are still large portions of electrons that will escape, the higher energy electrons. These electrons will go on to produce direct damage, if the nanoparticle is within a suitable distance. For the electrons that have a very short range after escaping the nanoparticle, the nanoparticle would need to be within several Å of the DNA. However, if the electron has a higher energy, this means it will travel a greater distance before depositing its energy, meaning the nanoparticle could be further away. The electrons that never make it to direct damage will also ionize particle along its path

length, and free radical generation will occur. These free radicals species have been studied, and cause great damage the DNA, as well. With this, even though not all the electrons are escaping from the nanoparticle, thermal energy will be created, which will also disrupt the physiological processes of the tumor cells, but indirect damage will occur.

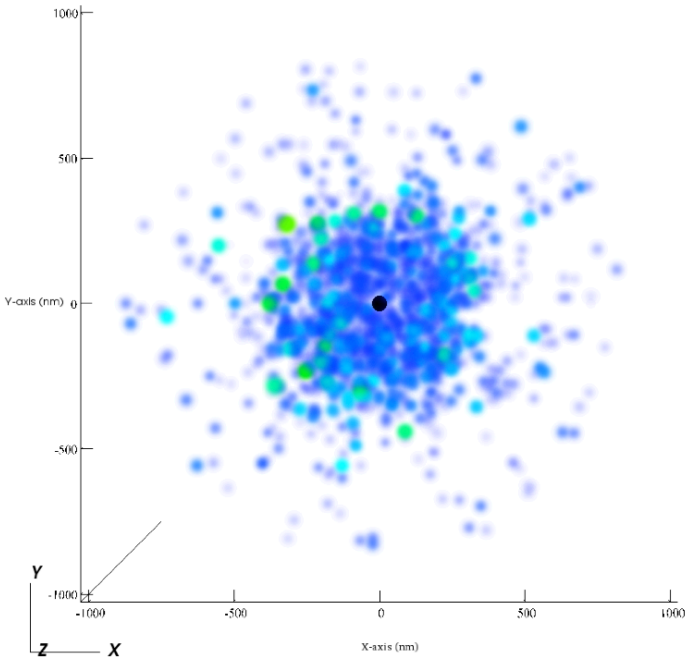

Figure 37. Free radical generation using G-values for radical species.

There are also free radicals generated from the interaction of the electrons with the water surrounding the nanoparticle, such as radical species from water radiolysis. The G-values for the radical species formed in Table 7 were used as functions in VisIt to

generate a visual representation of the radicals formed during the radioactive decay of ^{125}I. Figure 37 shows the values of the all the radical species combined.

4.6 Micro-metastasis Targeting

One of the challenges in cancer therapy is the lack of targeting associated with micro-metastases. Since these metastases cannot be readily detected, they cannot be treated effectively with current strategies. There are detection limitations associated with these specific metastases, as they are on the micro- scale and cannot be detected in CT scans, for example. Since they are so small, treatment is also not plausible. Regardless of the treatment modality chosen, there is not a way to achieve the cytotoxic dose of radiation needed to kill the tumor cells while leaving the majority of surrounding healthy tissue alive. This is a major problem in cancer therapy when it comes to micro metastases. While there are methods under review to improve targeting, such as CPPs, once we are able to reach a point in medicine where these micro metastases can be identified and located, any radionuclide and nanoparticle packaging would work well.

5. CONCLUSION

A decay of radioactive atoms contained within a gold nanoparticle was simulated using Geant4-DNA. These files were then used in VisIt, to visualize and analyze the results. From these studies, it was found where energy deposition occurred from Auger electron emissions of the two radionuclides used, ^{125}I and ^{117m}Sn. With this data, it could be determined how much damage to the DNA there would be.

The code simulated a single decay at a time. This is critical, as the nanoparticles only housed one radioactive atom. Most codes are not able to track particles down to extremely low energies, but as this is a "track structure" code, the results were detailed and contained all the pertinent information needed. The decay was sampled from the Geant4-DNA decay list, so all samples were independent and used actual energies, not averaged. Individually, the energies emitted are not averaged, and the structures within the cells will see discrete energy depositions, not averaged energy depositions. These results were validated with other sources.

It was also important in this work to compare the two radionuclides. Overall, ^{125}I would be the better choice for a radioactive nanoparticle, based on the results obtained.

For further work, I would simulate more radionuclides and focus on different particle emissions. Within Geant4-DNA, the radical generation and G-values could be analyzed more. From this analysis, the amount of radicals produced from the decay of ^{125}I and the higher energy electrons that would escape from ^{117m}Sn could be compared. Biological models could also be generated in Geant4-DNA, to accurately assess the number of strand breaks to the DNA. Modifications could be made to the actual

nanoparticle, including changing the location of the radioactive atom and changing the radius of the nanoparticle. It would also be beneficial to take these studies into the laboratory by synthesizing the gold nanoparticles and testing them in various situations.

REFERENCES

1. Ward BW, Schiller JS, Goodman RA, Multiple Chronic Conditions Among US Adults: A 2012 Update. Preventing Chronic Disease 2014; 11, E62.

2. Centers for Disease Control and Prevention, Death and Mortality. NCHS FastStats Web site. 2015.

3. Meropol NJ, Schrag D, Smith TJ, Mulvey TM, Langdon RM, Blum D, et al., American Society of Clinical Oncology Guidance Statement: The Cost of Cancer Care.; 2009.

4. Mariotto AB, Yabroff KR, Shao Y, Feuer EJ, Brown ML, Projections of the Cost of Cancer Care in the United States: 2010-2020. Journal of the National Cancer Institute 2011; 103, 117-28.

5. Siegel RL, Miller KD, Jemal A, Cancer Statistics, 2015. CA: A Cancer Journal for Clinicians 2015; 65, 5-29.

6. Cancer Facts and Figures 2014. Place American Cancer Society: American Cancer Society; 2014.

7. Weigelt B, Peterse JL, van 't Veer LJ, Breast Cancer Metastasis: Markers and Models. Nature Reviews Cancer 2005; 5, 591-602.

8. Kohler BA, Sherman RL, Howlader N, Jemal A, Ryerson AB, Henry KA, et al., Annual Report to the Nation on the Status of Cancer, 1975-2011, Featuring Incidence of Breast Cancer Subtypes by Race/Ethnicity, Poverty, and State. Journal of the National Cancer Institute 2015; 107.

9. Berman AT, Thukral AD, Hwang W-T, Solin LJ, Vapiwala N, Incidence and Patterns of Distant Metastases for Patients With Early-Stage Breast Cancer After Breast Conservation Treatment. Clinical Breast Cancer 2013; 13, 88-94.

10. Mullard A, 2012 FDA Drug Approvals. Nature Reviews Drug Discovery. 2013.

11. Gonzalez-Angulo AM, Morales-Vasquez F, Hortobagyi GN, Overview of Resistance to Systemic Therapy in Patients With Breast Cancer. Breast Cancer Chemosensitivty 2007; 608, 1-22.

12. D'Amico L, Roato I, The Impact of Immune System in Regulating Bone Metastasis Formation by Osteotropic Tumors. Journal of Immunology research 2015; 2015, 143526.

13. Hoskin P, Sartor O, O'Sullivan JM, Johannessen DC, Helle SI, Logue J, et al., Efficacy and Safety of Radium-223 Dichloride in Patients with Castration-Resistant Prostate Cancer and Symptomatic Bone Metastases, With or Without Previous Docetaxel Use: A Prespecified Subgroup Analysis from the Randomised, Double-Blind, Phase 3 ALSYMPCA Trial. The Lancet Oncology 2014; 15, 1397-406.

14. Nilsson S, Radium-223 Dichloride for the Treatment of Bone Metastatic Castration-Resistant Prostate Cancer: An Evaluation of its Safety. Expert Opinion on Drug Safety 2015, 1-10.

15. Bubendorf L, Schopfer A, Wagner U, Sauter G, Moch H, Willi N, et al., Metastatic Patterns of Prostate Cancer: An Autopsy Study of 1,589 Patients. Hum Pathol 2000; 31, 578-83.

16. Fusi A, Collette S, Busse A, Suciu S, Rietz A, Santinami M, et al., Circulating Melanoma Cells and Distant Metastasis-Free Survival in Stage III Melanoma Patients With or Without Adjuvant Interferon Treatment (EORTC 18991 side study). European Journal of Cancer (Oxford, England : 1990) 2009; 45, 3189-97.

17. Cook BE, The Use of Radioactive Nanoparticles for the Diagnosis and Treatment of Cancer. 2014.

18. Fisher ER, Fisher B, Experimental Study of Factors Influencing Development of Hepatic Metastases from Circulating Tumor Cells. Acta Cytol 1965; 9, 146-59.

19. A S Ketcham JJRHW, The Shredding of Viable Circulating Tumor Cells by Pulmonary Metastases in Mice. Annals of Surgery 1969; 169, 297.

20. Wexler H, Ryan JJ, Ketcham AS, The Study of Circulating Tumor Cells by the Formation of Pulmonary Embolic Tumor Growths in a Secondary Host. Cancer 1969; 23, 946-51.

21. Goodman OB, Jr., Fink LM, Symanowski JT, Wong B, Grobaski B, Pomerantz D, et al., Circulating Tumor Cells in Patients with Castration-Resistant Prostate Cancer Baseline Values and Correlation with Prognostic Factors. Cancer Epidemiol Biomarkers Prev 2009; 18, 1904-13.

22. Ma X, Xiao Z, Li X, Wang F, Zhang J, Zhou R, et al., Prognostic Role of Circulating Tumor Cells and Disseminated Tumor Cells in Patients with Prostate Cancer: A Systematic Review and Meta-Analysis. Tumour Biol 2014; 35, 5551-60.

23. Giesing M, Driesel G, Molitor D, Suchy B, Molecular Phenotyping of Circulating Tumour Cells in Patients with Prostate Cancer: Prediction of Distant Metastases. BJU international 2012; 110, E1202-11.
24. Bidard F-C, Peeters DJ, Fehm T, Nolé F, Gisbert-Criado R, Mavroudis D, et al., Clinical Validity of Circulating Tumour Cells in Patients with Metastatic Breast Cancer: A Pooled Analysis of Individual Patient Data. The Lancet Oncology 2014; 15, 406-14.

25. Yie S-m, Lou B, Ye S-r, He X, Cao M, Xie K, et al., Clinical Significance of Detecting Survivin-Expressing Circulating Cancer Cells in Patients with Non-Small Cell Lung Cancer. Lung Cancer (Amsterdam, Netherlands) 2009; 63, 284-90.

26. Cheng M, Liu L, Yang H-S, Liu G-F, Circulating Tumor Cells are Associated With Bone Metastasis of Lung Cancer. Asian Pacific Journal of Cancer Prevention : APJCP 2014; 15, 6369-74.

27. Igawa S, Gohda K, Fukui T, Ryuge S, Otani S, Masago A, et al., Circulating Tumor Cells As A Prognostic Factor in Patients With Small Cell Lung Cancer. Oncology Letters 2014; 7, 1469-73.

28. Tanaka F, Yoneda K, Kondo N, Hashimoto M, Takuwa T, Matsumoto S, et al., Circulating Tumor Cell As A Diagnostic Marker in Primary Lung Cancer. Clinical Cancer Research : An Official Journal of the American Association for Cancer Research 2009; 15, 6980-86.

29. Truini A, Alama A, Dal Bello MG, Coco S, Vanni I, Rijavec E, et al., Clinical Applications of Circulating Tumor Cells in Lung Cancer Patients by CellSearch System. Frontiers in Oncology 2014; 4, 242.

30. Khoja L, Lorigan P, Zhou C, Lancashire M, Booth J, Cummings J, et al., Biomarker Utility of Circulating Tumor Cells in Metastatic Cutaneous Melanoma. The Journal of Investigative Dermatology 2013; 133, 1582-90.

31. Kiyohara E, Hata K, Lam S, Hoon DSB, Circulating Tumor Cells as Prognostic Biomarkers in Cutaneous Melanoma Patients. Methods in Molecular Biology (Clifton, NJ) 2014; 1102, 513-22.

32. Medic S, Pearce RL, Heenan PJ, Ziman M, Molecular Markers of Circulating Melanoma Cells. Pigment Cell Research/Sponsored By the European Society for Pigment Cell Research and the International Pigment Cell Society 2007; 20, 80-91.

33. Mocellin S, Del Fiore P, Guarnieri L, Scalerta R, Foletto M, Chiarion V, et al., Molecular Detection of Circulating Tumor Cells is an Independent Prognostic Factor in Patients with High-Risk Cutaneous Melanoma. International Journal of Cancer 2004; 111, 741-45.

34. Wong IH, Chan AT, Johnson PJ, Quantitative Analysis of Circulating Tumor Cells in Peripheral Blood of Osteosarcoma Patients Using Osteoblast-Specific Messenger RNA Markers: A Pilot Study. Clinical Cancer Research: An Official Journal of the American Association for Cancer Research 2000; 6, 2183-88.

35. Tian Q, Jia J, Ling S, Liu Y, Yang S, Shao Z, A Causal Role for Circulating miR-34b in Osteosarcoma. European Journal of Surgical Oncology (EJSO) 2014; 40, 67-72.

36. DuBois SG, Stempak D, Wu B, Mokhtari RB, Nayar R, Janeway KA, et al., Circulating Endothelial Cells and Circulating Endothelial Precursor Cells in Patients with Osteosarcoma. Pediatric Blood & Cancer 2011; 58, 181-84.

37. Winters B, James A, Lee J, Kho J, Morrissey C, Wright J, Chemotherapeutic Effects on Circulating Tumor Cells in Bladder Cancer. International Journal of Urology: Official Journal of the Japanese Urological Association 2015.

38. Alva A, Friedlander T, Clark M, Huebner T, Daignault S, Hussain M, et al., Circulating Tumor Cells as Potential Biomarkers in Bladder Cancer. The Journal of Urology 2015.

39. Gazzaniga P, de Berardinis E, Raimondi C, Gradilone A, Busetto GM, De Falco E, et al., Circulating Tumor Cells Detection Has Independent Prognostic Impact in High-Risk Non-Muscle Invasive Bladder Cancer. International Journal of Cancer 2014; 135, 1978-82.

40. Nezos A, Pissimisis N, Lembessis P, Sourla A, Dimopoulos P, Dimopoulos T, et al., Detection of Circulating Tumor Cells in Bladder Cancer Patients. Cancer Treatment Reviews 2009; 35, 272-79.

41. Cegan M, Kolostova K, Matkowski R, Broul M, Schraml J, Fiutowski M, et al., In Vitro Culturing of Viable Circulating Tumor Cells of Urinary Bladder Cancer. International Journal of Clinical and Experimental Pathology 2014; 7, 7164-71.

42. Allen JE, Saroya BS, Kunkel M, Dicker DT, Das A, Peters KL, et al., Apoptotic Circulating Tumor Cells (CTCs) in the Peripheral Blood of Metastatic Colorectal Cancer Patients are Associated with Liver Metastasis But Not CTCs. Oncotarget 2014; 5, 1753-60.

43. Katoh S, Goi T, Naruse T, Ueda Y, Kurebayashi H, Nakazawa T, et al., Cancer Stem Cell Marker in Circulating Tumor Cells: Expression of CD44 Variant Exon 9 is Strongly Correlated to Treatment Refractoriness, Recurrence and Prognosis of Human Colorectal Cancer. Anticancer Research 2015; 35, 239-44.

44. Denève E, Riethdorf S, Ramos J, Nocca D, Coffy A, Daurès J-P, et al., Capture of Viable Circulating Tumor Cells in the Liver of Colorectal Cancer Patients. Clinical Chemistry 2013; 59, 1384-92.

45. Musella V, Pietrantonio F, Di Buduo E, Iacovelli R, Martinetti A, Sottotetti E, et al., Circulating Tumor Cells as a Longitudinal Biomarker in Patients with Advanced Chemorefractory, RAS-BRAF Wild-Type Colorectal Cancer Receiving Cetuximab or Panitumumab. International Journal of Cancer 2015.

46. Romiti A, Raffa S, Di Rocco R, Roberto M, Milano A, Zullo A, et al., Circulating Tumor Cells Count Predicts Survival in Colorectal Cancer Patients. Journal of Gastrointestinal and Liver Diseases : JGLD 2014; 23, 279-84.

47. Torino F, Bonmassar E, Bonmassar L, De Vecchis L, Barnabei A, Zuppi C, et al., Circulating Tumor Cells in Colorectal Cancer Patients. Cancer Treatment Reviews 2013; 39, 759-72.

48. Raimondi C, Nicolazzo C, Gradilone A, Giannini G, De Falco E, Chimenti I, et al., Circulating Tumor Cells: Exploring Intratumor Heterogeneity of Colorectal Cancer. Cancer Biology & Therapy 2014; 15, 496-503.

49. Vaiopoulos AG, Kostakis ID, Gkioka E, Athanasoula KC, Pikoulis E, Papalambros A, et al., Detection of Circulating Tumor Cells in Colorectal and Gastric Cancer Using a Multiplex PCR Assay. Anticancer Research 2014; 34, 3083-92.

50. Steinert G, Schölch S, Niemietz T, Iwata N, García SA, Behrens B, et al., Immune Escape and Survival Mechanisms in Circulating Tumor Cells of Colorectal Cancer. Cancer Research 2014; 74, 1694-704.

51. Huang X, Gao P, Song Y, Sun J, Chen X, Zhao J, et al., Meta-Analysis of the Prognostic Value of Circulating Tumor Cells Detected with the CellSearch System in Colorectal Cancer. BMC Cancer 2015; 15, 202.

52. Mostert B, Sieuwerts AM, Bolt-de Vries J, Kraan J, Lalmahomed Z, van Galen A, et al., mRNA Expression Profiles in Circulating Tumor Cells of Metastatic Colorectal Cancer Patients. Molecular Oncology 2015; 9, 920-32.

53. Lyberopoulou A, Aravantinos G, Efstathopoulos EP, Nikiteas N, Bouziotis P, Isaakidou A, et al., Mutational Analysis of Circulating Tumor Cells from Colorectal Cancer Patients and Correlation With Primary Tumor Tissue. PLoS ONE 2015; 10.

54. Mohamed Suhaimi N-A, Foong YM, Lee DYS, Phyo WM, Cima I, Lee EXW, et al., Non-Invasive Sensitive Detection of KRAS and BRAF Mutation in Circulating Tumor Cells of Colorectal Cancer Patients. Molecular Oncology 2015; 9, 850-60.

55. Divella R, Daniele A, Abbate I, Bellizzi A, Savino E, Simone G, et al., The Presence of Clustered Circulating Tumor Cells (CTCs) and Circulating Cytokines Define an Aggressive Phenotype in Metastatic Colorectal cancer. Cancer Causes & Control : CCC 2014; 25, 1531-41.

56. Sotelo MJ, Sastre J, Maestro ML, Veganzones S, Viéitez JM, Alonso V, et al., Role of Circulating Tumor Cells as Prognostic Marker in Resected Stage III Colorectal Cancer. Annals of Oncology 2015; 26, 535-41.

57. Chikarmane SA, Tirumani SH, Howard SA, Jagannathan JP, DiPiro PJ, Metastatic Patterns of Breast Cancer Subtypes: What Radiologists Should Know in the Era of Personalized Cancer Medicine. Clinical Radiology 2015; 70, 1-10.

58. Lee YT, Patterns of Metastasis and Natural Courses of Breast Carcinoma. Cancer Metastasis Reviews 1985; 4, 153-72.

59. Hayes DF, Cristofanilli M, Budd GT, Ellis MJ, Stopeck A, Miller MC, et al., Circulating Tumor Cells at Each Follow-Up Time Point During Therapy of Metastatic Breast Cancer Patients Predict Progression-Free and Overall Survival. Clinical Cancer Research: An Official Journal of the American Association for Cancer Research 2006; 12, 4218-24.

60. de Bono JS, Scher HI, Montgomery RB, Parker C, Miller MC, Tissing H, et al., Circulating Tumor Cells Predict Survival Benefit From Treatment in Metastatic Castration-Resistant Prostate Cancer. Clinical Cancer Research: An official Journal of the American Association for Cancer Research 2008; 14, 6302-09.

61. Kotz J, Nanoparticle-Based Imaging for Micrometastases : SciBX: Science-Business eXchange. SciBX: Science-Business eXchange 2011.

62. Liu TW, MacDonald TD, Jin CS, Gold JM, Bristow RG, Wilson BC, et al., Inherently Multimodal Nanoparticle-Driven Tracking and Real-Time Delineation of Orthotopic Prostate Tumors and Micrometastases. ACS Nano 2013; 7, 4221-32.

63. Fischer M, Kampen WU, Radionuclide Therapy of Bone Metastases. Breast Care 2012; 7, 100-07.

64. Kassis AI, Adelstein SJ, Radiobiologic Principles in Radionuclide Therapy. Journal of Nuclear Medicine 2005; 46, 4S-12S.

65. Kassis AI, The Amazing World of Auger Electrons. International Journal of Radiation Biology 2004.

66. Peiris PM, Toy R, Abramowski A, Vicente P, Tucci S, Bauer L, et al., Treatment of Cancer Micrometastasis Using a Multicomponent Chain-Like Nanoparticle. Journal Of Controlled Release 2014; 173, 51-58.

67. Zorko M, Langel Ü, Cell-Penetrating Peptides: Mechanism and Kinetics of Cargo Delivery. Advanced Drug Delivery Reviews 2005; 57, 529-45.

68. Zhang L, Lyer AK, Yang X, Kobayashi E, Guo Y, Mankin H, et al., Polymeric Nanoparticle-Based Delivery of microRNA-199a-3p Inhibits Proliferation and Growth of Osteosarcoma Cells. International Journal of Nanomedicine 2015; 10, 2913-24.

69. Chanda N, Kan P, Watkinson LD, Shukla R, Zambre A, Carmack TL, et al., Radioactive Gold Nanoparticles in Cancer Therapy: Therapeutic Efficacy Studies of GA-198AuNP Nanoconstruct in Prostate Tumor-Bearing Mice. Nanomedicine: Nanotechnology, Biology, and Medicine 2010; 6, 201-09.

70. Axiak-Bechtel SM, Upendran A, Lattimer JC, Kelsey J, Cutler CS, Selting KA, et al., Gum Arabic-Coated Radioactive Gold Nanoparticles Cause No Short-Term Local or Systemic Toxicity in the Clinically Relevant Canine Model of Prostate Cancer. International Journal of Nanomedicine 2014; 9, 5001-11.

71. Roy K, Lahiri S, A Green Method for Synthesis of Radioactive Gold Nanoparticles. Green Chemistry 2006; 8, 1063-66.

72. Balogh L, Minc L, Berka M, Novel Synthesis of Radioactive Gold/Dendrimer Composite Nanoparticles for the Treatment of Cancer. Nanomedicine: Nanotechnology 2007.

73. Chanda N, Kattumuri V, Shukla R, Zambre A, Katti K, Upendran A, et al., Bombesin Functionalized Gold Nanoparticles Show In Vitro and In Vivo Cancer Receptor Specificity. Proceedings of the National Academy of Sciences 2010; 107, 8760-65.

74. Kimling J, Maier M, Okenve B, Kotaidis V, Ballot H, Plech A, Turkevich Method for Gold Nanoparticle Synthesis Revisited. The Journal of Physical Chemistry B 2006; 110, 15700-07.

75. Katti KV, Kannan R, Katti K, Kattumori V, Pandrapraganda R, Rahing V, et al., Hybrid Gold Nanoparticles in Molecular Imaging and Radiotherapy. Czechoslovak Journal of Physics 2006; 56, D23-D34.

76. Shukla R, Chanda N, Zambre A, Upendran A, Katti K, Kulkarni RR, et al., Laminin Receptor Specific Therapeutic Gold Nanoparticles (198AuNP-EGCg) Show Efficacy in

Treating Prostate Cancer. Proceedings of the National Academy of Sciences 2012; 109, 12426-31.

77. Eblan MJ, Wang AZ, Improving Chemoradiotherapy With Nanoparticle Therapeutics. Translational Cancer Research 2013; 2, 320-29.

78. Li S, Goins B, Hrycushko BA, Phillips WT, Bao A, Feasibility of Eradication of Breast Cancer Cells Remaining in Postlumpectomy Cavity and Draining Lymph Nodes Following Intracavitary Injection of Radioactive Immunoliposomes. Molecular Pharmaceutics 2012; 9, 2513-22.

79. Mori H, Yasuda H, Alloy Phase Formation in Nanometer-Sized Particles. Materials Science and Engineering: A 2001; 312, 99-103.

80. Yasuda H, Furuya K, Spontaneous Alloying of Tin Atoms into Nanometer-Sized Gold Clusters and Phase Stability in the Resultant Alloy Clusters. The European Physical Journal D-Atomic, Molecular, Optical and Plasma Physics 2000; 10, 279-83.

81. Daniel M-C, Astruc D, Gold Nanoparticles: Assembly, Supramolecular Chemistry, Quantum-Size-Related Properties, and Applications Toward Biology, Catalysis, and Nanotechnology. Chemical Reviews 2004; 104, 293-346.

82. Cheng W, Dong S, Wang E, Iodine-Induced Gold-Nanoparticle Fusion/Fragmentation/Aggregation and Iodine-Linked Nanostructured Assemblies on a Glass Substrate. Angewandte Chemie (International ed in English) 2003; 42, 449-52.

83. Orlando TM, Meisel D, Radiation-Induced Processes in Aqueous Suspensions of Nanoparticles and Nanoscale Water Films: Relevance to H~2 Production in Mixed Waste and Spent Nuclear Fuel. 2001; 778, 284-98.

84. Meisel D, Charge Transfer in Nanoparticles. Studies in Surface Science and Catalysis 1997; 103, 79-97.

85. Zhang Z, Berg A, Levanon H, Fessenden RW, Meisel D, On the Interactions of Free Radicals with Gold Nanoparticles. Journal of the American Chemical Society 2003; 125, 7959-63.

86. Merga G, Milosavljevic BH, Meisel D, Radiolytic Hydrogen Yields in Aqueous Suspensions of Gold Particles. The Journal of Physical Chemistry B 2006; 110, 5403-08.

87. Ngwa W, Korideck H, Kassis AI, Kumar R, Sridhar S, Makrigiorgos GM, et al., In Vitro Radiosensitization by Gold Nanoparticles During Continuous Low-Dose-Rate Gamma Irradiation with I-125 Brachytherapy Seeds. Nanomedicine: Nanotechnology, Biology, and Medicine 2013; 9, 25-27.

88. Kassis A, Cancer Therapy with Auger Electrons: Are We Almost There? The Journal of Nuclear Medicine 2003.

89. Balagurumoorthy P, Xiang, X., Wang, K., Adelstein, J., Kassis, A., Effect of Distance Between Decaying 125I and DNA on Auger Electron Induced Double Strand Break Yield. Int J Radiat Biol 2012.

90. Balagurumoorthy P, Xu X, Wang K, Adelstein SJ, Kassis AI, Effect of distance between decaying 125I and DNA on Auger-electron induced double-strand break yield. International Journal of Radiation Biology 2012; 88, 998-1008.

91. Adelstein SJ, Kassis AI, Bodei L, Mariani G, Radiotoxicity of Iodine-125 and Other Auger-Electron-Emitting Radionuclides: Background to Therapy. Cancer Biotherapy & Radiopharmaceuticals 2003; 18, 301-16.

92. Duparc OH, Pierre Auger-Lise Meitner: Comparative Contributions to the Auger Effect. International Journal of Materials Research 2009; 100, 1162-66.

93. Hofer KG, Hughes WL, Incorporation of Iododeoxyuridine-125I into the DNA of L1210 Leukemia Cells During Tumor Development. Cancer Research 1970.

94. Nikjoo H, Girard P, Charlton DE, Hofer KG, Laughton CA, Auger electrons-A Nanoprobe for Structural, Molecular and Cellular Processes. 2007.

95. Bloomer WD, Adelstein SJ, Antineoplastic Effect of Iodine-125-Labelled Iododeoxyuridine. International Journal of Radiation Biology 1975.

96. Schwarz S, Thon, N., Nikolajek, K., Niyazi, M., Tonn, J., Belka, C., Kreth, F., Iodine-125 Brachytherapy for Brain Tumours-A Review. Radiation Oncology 2012.

97. Korb L, Brawer, M., Modern Brachytherapy for Localized Prostate Cancers: The Northwest Hospital (Seattle) Experience. Reviews in Urology 2001.

98. Stocklin G, Bromine-77 and Iodine-123 Radiopharmaceuticals. Int Journal of Applied Radiaiton and Isotopes 1977.

99. Braghirolli A, Waissmann, W., Silva, J., Santos, G., Production of Iodine-124 and its Applications in Nuclear Medicine. Applied Radiation and Isotopes 2014.

100. Joyce J, Swihart, A., Thyroid: Nuclear Medicine Update. Radiol Clin N Am 2011.

101. Charlton DE, Booz J, A Monte Carlo Treatment of the Decay of 125I. Radiation Research 1981; 87, 10-23.

102. Stevenson N, Production of Commerical High Specific Activity Sn-117m Radiochemical and Chelates. 2014.

103. Maslov OD, Starodub GY, Vostokin GK, Gustova MV, Dmitriev SN, Shvetsov VN, et al., Production of (117m)Sn with High Specific Activity by Cyclotron. Applied Radiation and Isotopes 2011; 69, 965-68.

104. Meesungnoen J, Jay-Gerin J-P, Filali-Mouhim A, Mankhetkorn S, Low-energy Electron Penetration Range in Liquid Water. Radiation Research 2002; 158, 657-60.

105. Kereiakes J, Rao, D., Auger Electron Dosimetry. AAPM 1992.

106. Emfietzoglou D, Nikjoo H, Accurate Electron Inelastic Cross Sections and Stopping Powers for Liquid Water Over the 0.1-10 keV Range Based on an Improved Dielectric Description of the Bethe surface. Radiation Research 2007; 167, 110-20.

107. Library LBN, X-ray Data Booklet; 2009.

108. Nguyen-Truong HT, Modified Bethe Formula for Low-Energy Electron Stopping Power Without Fitting Parameters. Ultramicroscopy 2015; 149, 26-33.

109. Joiner M, Kogel Avd, Basic Clinical Radiobiology. 4th ed. London: Hodder Arnold; 2009.

110. Le Caër S, Water Radiolysis: Influence of Oxide Surfaces on H2 Production Under Ionizing Radiation. Water 2011; 3, 235-53.

111. Hall E, Giaccia, A., Radiobiology for the Radiologist 2011.

112. Meesungnoen J, Benrahmoune M, Filali-Mouhim A, Mankhetkorn S, Jay-Gerin J-P, Monte Carlo Calculation of the Primary Radical and Molecular Yields of Liquid Water Radiolysis in the Linear Energy Transfer Range 0.3–6.5 keV/μm: Application to 137Cs Gamma Rays. Radiation Research 2001; 155, 269-78.

113. Terrissol M, Beaudre A, Simulation of Space and Time Evolution of Radiolytic Species Induced by Electrons in Water. Radiation Protection Dosimetry 1990.

114. Terrissol M, Peudon, A., Kummerle, E., Pomplun, E., On the Biological Efficiency of I-123 and I-125 Decay on the Molecular Level. Int J Radiat Biol 2008.

115. Bacq ZM, Chemical Protection Against Ionising Radiation. Triangle 1961; 5, 2-11.

116. Lazarakis P, Bug MU, Gargioni E, Guatelli S, Rabus H, Rosenfeld AB, Comparison of Nanodosimetric Parameters of Track Structure Calculated by the Monte

Carlo Codes Geant4-DNA and PTra. Physics In Medicine And Biology 2012; 57, 1231-50.

117. Francis Z, Incerti, S., Karamitros, M., Tran, H., Villagrasa, C., Stopping Power and Ranges of Electrons, Protons and Alpha Particles in Liquid Water Using the Geant4-DNA Package. Nuclear Instruments and Methods in Physics Research 2011.

118. Francis Z, Incerti S, Capra R, Mascialino B, Montarou G, Stepan V, et al., Molecular Scale Track Structure Simulations in Liquid Water Using the Geant4-DNA Monte-Carlo Processes. Applied radiation and isotopes 2011; 69, 220-26.

119. Champion C, Incerti, S., Karamitros, T., Shin, J., Lee, S., Lekadir, H., Bernal, M., Francis, Z., Ivanchenko, V., Fojon, O., Rivarola, R., Proton Transport in Water and DNA Components: A Geant4 Monte Carlo Simulation. Nuclear Instruments and Methods in Physics Research 2013.

120. Incerti S, Baldacchino G, Bernal M, Capra R, Champion C, Francis Z, et al., The Geant4-DNA project. International Journal of Modeling, Simulation, and Scientific Computing 2010; 1, 157-78.

121. Dos Santos M, Villagrasa, C., Clairand, I., Incerti, S., Influence of the DNA Density of the Number of Clustered Damages Created by Protons of Different Energies Nuclear Instruments and Methods in Physics Research 2013.

122. Chauvie S, Francis Z, Guatelli S, Incerti S, Mascialino B, Moretto P, et al., Geant4 Physics Processes for Microdosimetry Simulation: Design Foundation and Implementation of the First Set of Models. Nuclear Science, IEEE Transactions on 2007; 54, 2619-28.

123. Madsen JR, Akabani G, Low-Energy Cross-Section Calculations of Single Molecules by Electron Impact: A Classical Monte Carlo Transport Approach With Quantum Mechanical Description. Physics In Medicine And Biology 2014; 59, 2285-305.

124. Francis Z, Incerti S, Ivanchenko V, Champion C, Karamitros M, Bernal MA, et al., Monte Carlo Simulation of Energy-Deposit Clustering for Ions of the Same LET in Liquid Water. Physics In Medicine And Biology 2012; 57, 209-24.

125. Bernal M, Sikansi, D., Cavalcante, F., Incerti, S., Champion, C., Ivanchenko, V., An Atomistic Geometrical Model of the B-DNA Configuration for DNA–Radiation Interaction Simulations. Computer Physics Communications 2013.

126. Agostinelli S, Foppiano, F., Garelli, S., Paoli, G., The Application of Geant4 Simulation Code for Brachytherapy Treatment. European Organization for Nuclear Research 2000.

127. Rodrigues P, Moura, R., Ortigao, C., Peralta, L., Pia, M., Trindade, A., Varela, J., Geant4 Applications and Developments for Medical Physics Experiments. IEEE Transactions on Bio-Medical Engineering 2004.

128. Vassiliev ON, Electron Slowing-Down Spectra in Water for Electron and Photon Sources Calculated with the Geant4-DNA Code. Physics In Medicine And Biology 2012; 57, 1087-94.

129. Incerti S, Ivanchenko A, Karamitros M, Mantero A, Moretto P, Tran HN, et al., Comparison of GEANT4 Very Low Energy Cross Section Models With Experimental Data in Water. Medical Physics 2010; 37, 4692-708.

130. Villagrasa C, Francis Z, Incerti S, Physical Models Implemented in the Geant4-DNA extension of the Geant-4 Toolkit for Calculating Initial Radiation Damage at the Molecular Level. Radiation Protection Dosimetry 2011; 143, 214-18.

131. Champion C, Incerti S, Perrot Y, Delorme R, Bordage MC, Bardiès M, et al., Dose Point Kernels in Liquid Water: An Intra-Comparison Between Geant4-DNA and a Variety of Monte Carlo Codes. Applied Radiation and Isotopes 2014; 83 Pt B, 137-41.

132. Bernal MA, deAlmeida CE, Sampaio C, Incerti S, Champion C, Nieminen P, The Invariance of the Total Direct DNA Strand Break Yield. Medical Physics 2011; 38, 4147-53.

133. Seo H, Pia, M., Saracco, P., Kim, C., Ionization Cross Sections for Low Energy Electron Transport. IEEE Transactions on Bio-Medical Engineering 2011.

134. Abolfath RM, Carlson DJ, Chen ZJ, Nath R, A Molecular Dynamics Simulation of DNA Damage Induction by Ionizing Radiation. Physics In Medicine And Biology 2013; 58, 7143-57.

135. Hauf S, Kuster M, Pia MG, Bell Z, Briel U, Chipaux R, et al., Progress and Validation of Geant4 Based Radioactive Decay Simulation Using the Examples of Simbol-X and IXO. 2009 IEEE Nuclear Science Symposium and Medical Imaging Conference (NSS/MIC 2009). Place IEEE: IEEE; 2009.

136. Hauf S, Kuster M, Batic M, Bell ZW, Hoffmann DHH, Lang PM, et al., Radioactive Decays in Geant4. Ieee Transactions On Nuclear Science 2013; 60, 2966-83.

137. Nikjoo H, Martin RF, Charlton DE, Terrissol M, Kandaiya S, Lobachevsky P, Modelling of Auger-induced DNA Damage by Incorporated 125I. Acta Oncologica (Stockholm, Sweden) 1996; 35, 849-56.

138. Hainfeld JF, Dilmanian FA, Slatkin DN, Smilowitz HM, Radiotherapy Enhancement with Gold Nanoparticles. Journal of Pharmacy and Pharmacology 2008; 60, 977-85.

139. Jones BL, Krishnan S, Cho SH, Estimation of Microscopic Dose Enhancement Factor Around Gold Nanoparticles by Monte Carlo Calculations. Medical Physics 2010; 37, 3809-16.

140. Cho SH, Estimation of Tumour Dose Enhancement Due to Gold Nanoparticles During Typical Radiation Treatments: A Preliminary Monte Carlo Study. Physics In Medicine And Biology 2005; 50, N163-N73.

141. Chow JCL, Leung MKK, Fahey S, Chithrani DB, Jaffray DA, Monte Carlo Simulation on Low-Energy Electrons from Gold Nanoparticle in Radiotherapy. Journal of Physics: Conference Series 2012; 341, 012012.

142. Townley HE, Rapa E, Wakefield G, Dobson PJ, Nanoparticle Augmented Radiation Treatment Decreases Cancer Cell Proliferation. Nanomedicine : Nanotechnology, Biology, and Medicine 2012; 8, 526-36.

143. Townley HE, Kim J, Dobson PJ, In Vivo Demonstration of Enhanced Radiotherapy Using Rare Earth Doped Titania Nanoparticles. Nanoscale 2012; 4, 5043-50.

144. Roeske JC, Nunez L, Hoggarth M, Labay E, Weichselbaum RR, Characterization of the Theorectical Radiation Dose Enhancement from Nanoparticles. Technology in Cancer Research & Treatment 2007; 6, 395-401.

145. Robar JL, Riccio SA, Martin MA, Tumour Dose Enhancement Using Modified Megavoltage Photon Beams and Contrast Media. Physics In Medicine And Biology 2002; 47, 2433-49.

146. Prezado Y, Fois G, Le Duc G, Bravin A, Gadolinium Dose Enhancement Studies in Microbeam Radiation Therapy. Medical Physics 2009; 36, 3568-74.

147. Mesbahi A, A Review on Gold Nanoparticles Radiosensitization Effect in Radiation Therapy of Cancer. Reports of Practical Oncology and Radiotherapy: Journal of Greatpoland Cancer Center in Poznań and Polish Society of Radiation Oncology 2010; 15, 176-80.

148. Montenegro M, Nahar SN, Pradhan AK, Huang K, Yu Y, Monte Carlo Simulations and Atomic Calculations for Auger Processes in Biomedical Nanotheranostics. The Journal of Physical Chemistry A 2009; 113, 12364-69.

149. Zhang DG, Feygelman V, Moros EG, Latifi K, Zhang GG, Monte Carlo Study of Radiation Dose Enhancement by Gadolinium in Megavoltage and High Dose Rate Radiotherapy. PLoS ONE 2014; 9, e109389.

150. Pomplun E, Sutmann G, Is Coulomb Explosion a Damaging Mechanism for (125)IUdR? International Journal of Radiation Biology 2004; 80, 855-60.

151. Kümmerle EA, Pomplun E, Charge Build-Up During Decay of DNA-Incorporated (123/125)I: Consequences for Labeled Molecular Structures. International Journal of Radiation Biology 2012; 88, 922-27.

152. Humm JL, Howell RW, Rao DV, Dosimetry of Auger-Electron-Emitting Radionuclides: Report No. 3 of AAPM Nuclear Medicine Task Group No. 6. Medical Physics 1994; 21, 1901-15.

153. Pavlicek W, Walton, H., Karstaedt, P., Gray, R., Radiation Safety With Use of I-125 Seeds for Localization of Nonpalpable Breast Lesions. Acad Radiol 2006.

154. deGuzman A, Kearns, W., Shaw, E., Tatter, S., Stieber, V., Yates, C., Amadeo, H., Hinson, W., Radiation Safety Issues with High Activities of Liquid I-125: Techniques and Experience. Journal of Applied Clinical Medical Physics 2003.

155. Sisson J, McDougall, I., Dauer, L., Hurley, J., Brierley, J., Edinboro, C., Rsenthal, et. al., Radiation Safety in the Treatment of Patients with Thyroid Diseases by Radioiodine 131I: Practice Recommendations of the American Thyroid Association. The American Thyroid Association Taskforce on Radioiodine Safety 2011.

156. Lee J, Choi, K., Yu, K., Surface Treatments of Silver Rods with Enhanced Iodide Adsorption for I-125 Brachytherapy Seeds. Applied Radiation and Isotopes 2014.

157. Dreaden E, Alkilany, A., Huang, X., Murphy, C., The Golden Age: Gold Nanoparticle for Biomedicine. Chem Soc Rev 2012.